Spatial and Temporal Extrapolation of Disdrometer Size Distributions Based on a Lagrangian Trajectory Model of Falling Rain

John E. Lane
ASRC Aerospace
Kennedy Space Center, FL 32899

Takis Kasparis
Dept. of Electrical Eng. and Information Technologies
Cyprus Univ. of Technology, Limassol, Cyprus

W. Linwood Jones
School of Electrical Engineering and Computer Science
Univ. of Central Florida, Orlando, FL 32816

Philip T. Metzger
NASA/KSC Granular Mechanics and Surface Physics Lab
Kennedy Space Center, FL 32899

ABSTRACT

Methodologies to improve disdrometer processing, loosely based on mathematical techniques common to the field of particle flow and fluid mechanics, are examined and tested. The inclusion of advection and vertical wind field estimates appear to produce significantly improved results in a Lagrangian hydrometeor trajectory model, in spite of very strict assumptions of non-interacting hydrometeors, constant vertical air velocity, and time independent advection during the scan time interval. Wind field data can be extracted from each radar elevation scan by plotting and analyzing reflectivity contours over the disdrometer site and by collecting the radar radial velocity data to obtain estimates of advection. Specific regions of disdrometer spectra (drop size versus time) often exhibit strong gravitational sorting signatures, from which estimates of vertical velocity can be extracted. These independent wind field estimates become inputs and initial conditions to the Lagrangian trajectory simulation of falling hydrometeors.

INTRODUCTION

Most precipitation reaching the ground in the tropics does so in the form of raindrops and occasionally hail. From a very simplistic point of view, these hydrometeors can be viewed as non-interacting and falling at a constant terminal velocity. Even though this assumption is not generally accurate, because of the many physical processes such as break-up, evaporation, and coalescence, it is nevertheless a useful assumption for the purpose of analyzing many important properties of rainfall. A one-way coupled two-phase system approach for computing the dynamics of particles in a fluid system is standard practice when two-way coupling is not practical. For example, the interaction of aerosol droplets in a compressed gas stream may be, to first order, predicted by modeling the trajectories of individual non-interacting droplets propelled by a gas that is unaffected by the presence of the droplets. A similar methodology can be used to approach analysis of hydrometeor trajectories which may be highly influenced by the fluid motion of the ambient air.

The convention adopted in this work to describe the ambient air motion is to imply a cylindrical coordinate system so that wind vector at every point in space is composed of a horizontal and a vertical component. Keeping with the meteorological convention, the horizontal wind component is referred to as the *advection* velocity, while the vertical component is referred to as the *updraft* velocity (for a positive vertical motion), or *downdraft* velocity (for a negative vertical velocity).

DISDROMETER GRAVITATION SORTING SIGNATURE

The primary motivation for this work at the start was the observation and subsequent attempt to model gravitational sorting of raindrops in disdrometer spectra data. Gravitational sorting observations in disdrometer data have been reported in the literature on numerous occasions, but it is not a common observation simply because of the way in which disdrometer data is typically stored and plotted. The *gravitational sorting* (GS) signature is best observed when every drop impact measured by the disdrometer is time tagged and then displayed as a scatter plot of drop diameter D vs. time t. The resulting D-t plots often show marked diagonal features, where these GS features are always characterized by a negative slope when plotted as D vs. t. This can be explained by a simplistic model of non-interacting drops traveling at terminal velocity v_D as a function of drop diameter D, along with an ambient vertical wind motion w. At a time $t = t_0$, a pulse of rain characterized by a typical *drop size distribution* (DSD), such as the Marshall Palmer (MP) (Marshall, 1948) or gamma distribution (see Appendix A), starts at a height h above the ground site where a disdrometer is acquiring raindrop spectra (i.e., counting and measuring drop sizes). The height h is an idealized point of rainfall generation where a rainfall DSD, such as the MP DSD at $z = h$, completely determines the size distributions of falling drops. This point should be correlated to a level within a cloud where rainfall begins its unimpeded trek to the ground, such as the 0° C isotherm.

Other hydrometeor p can be treated similarly, but some significant difficulties with mixed phases (rain, hail, etc.) are encountered because of factors such as overlap in size distributions (small hail may be larger than large rain drops); differences in terminal velocities (round hail versus flattened rain drops); and differences in radar reflectivity (ice has a somewhat higher radar reflectivity than rain for equivalent scattering cross-sections).

The GS disdrometer signature can be modeled based on the simplifying assumption of non-interacting drops by first expressing the hydrometeor fall time as:

$$\tau_D = h/(v_D - w) \tag{1}$$

where $\tau_D = t_D - t_0$ is the fall time of a hydrometeor of diameter D, t_D is the clock time of the disdrometer recorded hit, v_D is the terminal velocity, and w is the vertical air motion. An estimate of terminal velocity reasonable for drop sizes associated with normal rain, is $v_D \approx aD^b$, where $a \approx 4.5$ [m s^{-1} mm^{-b}], and $b = 1/2$. Substituting this expression into Equation (1) and solving for the drop diameter D, results in:

$$D = \begin{cases} \left(\dfrac{h/\tau_D + w}{a}\right)^{1/b} & h/\tau_D + w > 0 \\ \textit{undefined} & h/\tau_D + w \le 0 \end{cases} \tag{2}$$

Figures 1 and 2 show Equation (2) plotted for various values of h and w. Equation (2) is an idealized description of gravitational sorting raindrops due to a zero width rain pulse (delta function). Figure 3 is a Monte Carlo simulation of raindrops generated by 60 [s] pulse width MP DSD. The simulated disdrometer data of Figure 3 differs from the real disdrometer data of Figure 4 for several reasons, to be discussed later.

The vertical feature shown in the $h = 0$ case on the left side of Figure 3, can also occur for $w \to -\infty$, where the raindrops generated at h and $t = t_0$ are swept downward by infinite velocity downdraft to appear immediately at the ground to be recorded by the disdrometer. Neither the $h = 0$ or $w \to -\infty$ cases are physical cases, but serve as a convenient means to test and exercise the simulations.

Pulsed rainfall is commonly found in convective cells and thunderstorms where large variations of the time dependence of rainfall rate are common, where the most extreme case is a square pulse in both time and space. The GS signature is less common in the case of stratiform rainfall because the time derivative of rainfall rate is small so that no pulse-like conditions are observed. The *D-t* character shown on the left side of Figure 3 (the $h = 0$ case), occurs commonly in real disdrometer data when the rainfall rate is constant. It is also somewhat common to see the sharp discontinuities of *D-t* as shown in this simulation. This feature can occur during convective rainfall or stratiform rain due to advection. Advection causes the rainfall source, which is of finite extent, such as a convective cell, to pass over the disdrometer. In that case, the sharpness of the start and stop of the *D-t* scatter plot is due the sharpness of the spatial extent of the rainfall source.

Figure 4 shows disdrometer data from the UCF Joss site in Orlando, FL (lat: 28.6016, lon: -81.1986), corresponding to September 30, 2008, from approximately 19:00 – 21:00 UTC. Even thought the individual drops impacts are not time tagged in the Joss data, the stored histogram size interval and time interval are sufficiently small to generate a *D-t* scatter plot. The count in the histogram drop size-time interval is plotted as a *density plot* in Figure 4 such that a higher count in the histogram bin appears as a darker spot on the plot. Near the end of the rainfall event, GS features due to pulsed rain become clearly evident. Equation (2) is manually fitted to several of these features and overlaid on the plot.

DISDROMETER DERIVED RAINFALL PRODUCTS

From the disdrometer histogram, an equivalent drop size distribution can be immediately computed:

$$\textit{Drop Size Distribution}: \qquad N_{jk} = \frac{H_{jk}}{v_{D_j} A_S \Delta t \Delta D} \tag{3}$$

$$\textit{Rainfall Rate}: \qquad R_k = \frac{\pi}{6 A_S \Delta t} \sum_{j=1}^{M} D_j^3 H_{jk} \tag{4}$$

$$\textit{Reflectivity}: \qquad Z_k = \frac{1}{A_S \Delta t} \sum_{j=1}^{M} \frac{D_j^6}{v_{D_j}} H_{jk} \tag{5}$$

where H_{jk} is the Joss disdrometer generated histogram corresponding to elapsed time $k\Delta t$ and drop size D_j; A_S is the Joss sensor area equal to 50 [cm^2]; and v_{D_j} is the terminal velocity (see Appendix) corresponding to drop diameter size D_j. In Figure 4, $\Delta t = 10$ [s] and the histogram has been resampled to a uniform diameter size so that $\Delta D = 0.1$ [mm] and $D_j = j\Delta D$. In Figure 5, $\Delta t = 30$ [s] and D_j is based on the Joss table of $M = 127$ non-uniformly spaced diameter sizes.

RADAR DATA

The Melbourne NWS radar is located approximately 55 [km] to the southeast of the UCF Joss site. For purposes of this study, radar data in only the lowest four scan elevations will be processed, and only in a 4x4 [km] horizontal extent centered over the Joss site. This region is later expanded to 8x8 [km] in order to extract the advection velocity. For the majority of this analysis, the radar reflectivity data is plotted in a pseudo 3D format, referred to as *3DRadPlot* (see Appendix B). This display format was adopted and utilized in the study of hail events surrounding the Pad 39B structure at the Kennedy Space Center (Lane, 2008). The same format is useful in analyzing the UCF Joss disdrometer data.

The basis of *3DRadPlot* display processing is based on a simplified and customized version of Shepard's interpolation formula (Shepard, 1969). For any point in space, the interpolated reflectivity $Z(\mathbf{r})$ at $\mathbf{r} = \{x, y, z\}$ is due to the weighted average of all reflectivity data points Z_i at the center of all radar bin locations $\mathbf{r}_i$ in the local region:

$$Z(\mathbf{r}) = \frac{\sum_{i=1}^{N} Z_i \left|\mathbf{r} - \mathbf{r}_i\right|^{-p}}{\left|\mathbf{r} - \mathbf{r}_i\right|^{-p}} \tag{6}$$

where N is the number of reflectivity data points used in the interpolation, for example, $N = 48$, the number of circles in Figure 6 (the number of radar bins in the region defined by 4x4 [km] x 4 scan elevations). The exponent parameter p controls the rate of transition between actual data points and the interpolated values. The larger this value, the sharper the transition between actual values defined by $\mathbf{r}_i$. In this work, a value of $p = 8$ was used throughout. Figures 7 and 8 are examples of *3DRadPlot* outputs of reflectivity for 19:23 UTC and 19:38 UTC respectively. This can be compared to the reflectivity derived from the Joss as shown in Figure 5 (more on this topic below).

JOSS DERIVED PRODUCTS

Figure 9 is a Joss histogram corresponding to Figure 4, summed over all k time intervals. This in itself is not a terribly useful product, but it is easy to generate and may be serve as a convenient method of categorization of rainfall events. The formal drop size distribution specified by Equation (3) is a much more useful quantity in comparing rainfall events, especially since it is normalized by time. Figure 10 is the Joss derived drop size distribution using Equation (3), for the entire storm event of Figure 4, with $\Delta t = 6000$ [s]. The MP DSD equivalent corresponds to an average rainfall rate of 10 [mm h^{-1}]. Since the length of the storm event may be ambiguous, it is preferable to define shorter time intervals and then generating multiple DSDs as a function of

time. Of course the classic method promoted in the work of Marshall and Palmer is to group the DSDs by rainfall rate as opposed to time.

Figure 11 is a comparison of the Joss derived rainfall rate from Equation (4) $\Delta t = 30$ [s] (thick line) and the rainfall rate from three collocated rain gauges (thin lines). The Joss and three rain gauges are clustered together within a 5 [m] diameter area on the roof of the UCF Engineering building in Orlando, FL. The total storm accumulated gauge rainfall average is 19.39 [mm], as compared to the 16.26 [mm] for the Joss. The cause of this 16% difference in rainfall accumulation between the Joss and rain gauges is not known. Suspected causes may be interfering wind on the roof of the building under conditions of high rainfall rate, or a disdrometer that is in need of calibration. This discrepancy is larger than it should be, but it is not the topic of this work and will not interfere significantly with the results presented in this paper. In future work however, we would hope to have a better initial correlation between disdrometer derived rainfall rate and collocated rain gauge data.

Figure 12 is close-up of disdrometer derived reflectivity for the lowest four elevation scans over the UCF site (refer to Figure 6) with time marks for 19:23 UTC and 19:38 UTC scans. The average disdrometer Z for 19:23 UTC is 50.1 dBZ and 43.9 dBZ for 19:38 UTC when averaging over the two sets of four elevation scan time marks. The radar reflectivity of Figure 7 for 19:23 UTC is ~ 45 dBZ, about 5 dBZ lower than the disdrometer derived value. The radar reflectivity shown in Figure 8 for 19:38 UTC is ~ 30 dBZ, about 14 dBZ lower than the disdrometer derived value. Proposing and testing and explanatyion for these kind of discrepancies is the goal of this work. The remainder of the material presented in this paper addresses this issue. The solution strategy takes into account the GS observations in the disdrometer data. It also should be noted at this time that final strategies for improving the disdrometer derived radar reflectivity will involve tactics that will ultimately be used to compute the disdrometer extrapolated 4D-DSD (a function of x, y, z, t, and D). Then, all disdrometer products can be computed from the 4D-DSD, including the equivalent radar reflectivity based on the 6^{th} moment of the 4D-DSD.

INCORPORATION OF DROP FALL TIME

Figure 13 depicts three methodologies for computing disdrometer derived reflectivity. The first method in Figure 13a is simply the direct application of Equation (4), as was demonstrated in the previous section for the 19:23 UTC radar scan, in which case a 5 dBZ discrepancy was observed between the disdrometer and radar reflectivites. Figure 13b illustrates an improvement to this simple case in which a time delay is applied to compensate for the average fall time from the height of the center of the radar bin based on an average drop terminal velocity. This intermediate case is presented without an example because our real interest is the third case of Figure 13c. This is the *GS time delay* case where the disdrometer time delay is based on gravitational sorting from Equation (1) and is dependent on the terminal velocity v_D of each drop size as well as the vertical air motion w. The examples to be examined will now be based on comparing the simple case of Figure 13a and two case from Figure 13c, one with $w = 0$ and one with w chosen to enforce a good comparison (in a least squares sense) between the disdrometer Z' and the radar Z. In order to incorporate Equation (1), the computation of disdrometer derived reflectivity, from Equation (5), must be modified:

$$Z_k = \frac{1}{A_S \Delta t} \sum_{\substack{j=1 \\ v_{D_j} > w}}^{M} \frac{D_j^6}{v_{D_j}} H_{jk'} \tag{7a}$$

$$k'\Delta t = k\Delta t + Int[\tau_D]$$

$$k' = k + \begin{cases} Int\left[\dfrac{z}{(v_{D_j} - w)\Delta t}\right] & v_{D_j} > w \\ undefined & v_{D_j} \le w \end{cases} \tag{7b}$$

The presence of v_D in Equation (7b) implies that the index k' in Equation (7a) is a function of index j, which depends on the details of the terminal velocity approximation used. Note the vertical air velocity is not used in Equation (7a) since it is assumed that the vertical air motion is zero near the ground, and up the height that is required to reach terminal velocity. So then for the largest drop sizes, it is assumed that vertical air motion is zero within a vertical region extending to 10 to 20 [m] above the disdrometer. Otherwise, Equation (7a) would need to be modified to account for the effect of vertical air movement on drop velocities at the disdrometer.

The summation must be constrained on several fronts. To examine this in more detail, we will need to pick an explicit form of v_D. Using the drop terminal velocity from a previous section, $v_D \approx aD^b$, and replacing D with the discrete value $D_j = j\Delta D$, results in:

$$k' = k + \begin{cases} Int\left[\dfrac{z}{(a\Delta D^b j^b - w)\Delta t}\right] & j > j_0 \\ undefined & j \le j_0 \end{cases} \tag{8}$$

Equation (7a) may now be expressed in terms of the drop size index j as:

$$\begin{aligned} Z_k &= \frac{1}{A_S a \Delta t} \sum_{j=j_0}^{M} \frac{(j\Delta D)^6}{(j\Delta D)^b} H_{jk'} \\ &= \frac{\Delta D^{6-b}}{A_S a \Delta t} \sum_{j=j_0}^{M} j^{6-b} H_{jk'} \end{aligned} \tag{9a}$$

where,

$$j_0 = 1 + \begin{cases} Int\left[\dfrac{w^{\frac{1}{b}}}{a^{\frac{1}{b}}\Delta D}\right] & w > 0 \\ 0 & w \le 0 \end{cases} \tag{9b}$$

and since the sum in Equation (9a) is truncated for $j \le j_0$, the time delayed index k' can be written as:

$$k' = k + Int\left[\frac{z}{(a\Delta D^b j^b - w)\Delta t}\right] \tag{9c}$$

Equations (9) define an algorithm to compute a disdrometer derived reflectivity that accounts for drop fall time due to terminal velocity as well as vertical air motion, corresponding to the case depicted in Figure 13c. Equations (9) an be forced to reduce to the simple case of Figure 13a and Equation (5), by letting $w \to -\infty$. The result is that $k' \to k$ and $j_0 \to 1$, so that Equation (9a) reduces to Equation (5). Physically, this would represents a hypothetical infinite downdraft which transports the drops to the ground at the disdrometer in zero time, so that the radar reflectivity then corresponds to the disdrometer derived reflectivity. This absurd hypothetical case highlights the equally absurd basis of applying the simple case of Figure 13a and Equation (5) for comparing disdrometer reflectivity to radar reflectivity.

An additional limit that needs to be noted is due to the finite length of H_{jk} in the k direction (discrete time axis). k' from Equation (9c) can exceed this extent under several conditions. When this occurs, the summation in Equation (9c) must simply be truncated or H_{jk} set to zero for those values of k'.

Table 1 compares the UCF Joss disdrometer derived reflectivity corresponding to consecutive radar scans from 19:04 – 19:38 UTC, on September 30, 2008. The 3DRadPlot format is utilized for easy comparison of the volume scan reflectivity in a 2x2x1 [km] box centered over the Joss disdrometer. Note that because of the geometry, only the lowest elevation scan will have a significant impact on the displayed reflectivity, even though all points in the lowest four scans are used (as illustrated in Figure 6) in the Shepard (1968) interpolation. Recall that the disdrometer data is resampled to a constant drop size bin width, with $\Delta D = 0.1[mm]$, and the original sample time, $\Delta t = 10[s]$ are used in Equations (9).

In order to obtain a more meaningful comparison with radar, disdrometer Z is computed via Shepards interpolation at all of the radar bin points shown in Figure 6, with the actual height values z and time of scan defined by index k. Note that the exact positions of those points are contained in the Level III product data file and change position from volume scan to volume scan. The first column is disdrometer Z using the simple case of Figure 13a and Equation (5), however it is calculated by the numerically equivalent method of setting w = -999 in Equations (9). The second column is computed similarly as the first column, but with $w = 0$. The third column is computed by choosing a w that gives the best (very subjective) overall match to the radar data of the last column. In general, there is an improvement from left to right. In some case, for example the 19:38 UTC scan, the first to columns are drastically off from the radar data, but a empirical guess at $w = 6.5$ [m s^{-1}] results in a good comparison.

Consideration of horizontal advection as well as drop vertical fall time provides additional improvement in the calculation of disdrometer reflectivity, as will be shown in the following section.

INCORPORATION OF CLOUD ADVECTION EFFECTS

In this approach, radar reflectivity and radial velocity data are used in addition to disdrometer spectra, where the end goal is no longer just a improved comparison between radar Z and disdrometer Z. The goal is to arrive at a good prediction of the DSD as a function of all three spatial coordinates, as well as time. Once that is accomplished, the resulting 4D-DSD can then be used to calculate rainfall products, analogous to Equations A.18 – A.26 of Appendix A. Never-the-less, it is still convenient and useful to compare the final disdrometer derived reflectivity from the 6th moment of the 4D-DSD to the corresponding radar reflectivity.

Even though there are typically four dozen radar bin locations at each complete scan in the 2x2x1 [km] volume surrounding the UCF disdrometer site as shown in Figure 6, far fewer than that number contribute significantly to the estimate of the 4D-DSD, primarily those in the lowest elevation scan. Based on Figure 6, there are a half dozen especially influential points. Therefore, the number of free and arbitrary model fitting parameters should not be allowed to exceed the number of radar reflectivity points in order to properly satisfy least squares fitting requirements. However, this is more of a intelligent guideline than a strict rule since the approach taken in this work is not to implement a stringent least squares comparison of radar and disdrometer *Z*.

Table 2 shows the Melbourne NEXRAD radial velocity over the disdrometer site for several scans of the example rainfall event for the first three elevations. This data was acquired using the NOAA Weather and Climate Toolkit, version 2.2, from the National Climatic Data Center (a free software download). Note that both *classified* (velocity quantized to multiple of 5 [kts]) and *unclassified* data are shown in Table 2. The important characteristic to note in this data is the sometimes strong vertical gradient of the horizontal winds. This feature is most notable at the beginning of the storm where many atmospheric processes may interact, such as gust fronts and sea breeze collisions, as well as strong updrafts and downdrafts. On the backside of the storm (last two rows of Table 2), the vertical gradient is small or non-existent.

An empirical advection model that is both relevant to the 4D-DSD volume and consistent with the observations of vertical advection gradients in the NEXRAD radial velocity, was used in this work:

$$\mathbf{u}(z) = \left(\gamma + (1-\gamma) \tanh \frac{z - z0}{L_z} \right) \mathbf{u}_0 \tag{10a}$$

with,

$$\mathbf{u}_0 = u_0 \begin{pmatrix} \cos\psi \\ \sin\psi \end{pmatrix} \tag{10b}$$

The model described Equation (10) exhibits two asymptotic values: $\mathbf{u}(z) \to (2\gamma - 1)\mathbf{u}_0$ for $(z - z_0)/L_z << 0$ and $\mathbf{u}(z) \to \mathbf{u}_0$ for $(z - z_0)/L_z >> 0$. The center of the transition at $z = z_0$ is $\mathbf{u}(z) = \gamma\,\mathbf{u}_0$ and the rate of the transition between asymptotic values is controlled by the parameter L_z. The 4D-DSD model is implemented in a Cartesian coordinate system with positive *x* pointing east, positive *y* pointing north, and positive *z* pointing up. Therefore, advection angle ψ adheres to the polar angle convention of the Cartesian system so that $\psi = 0$ simulates an advection travelling from west to east, $\psi = 90°$ simulates an advection travelling from south to north, and so on.

A simulated radial velocity can be calculated from Equation (10a) by performing the vector dot product with the radar direction vector:

$$U_r(z) = \begin{pmatrix} \cos\theta\cos\phi \\ \cos\theta\sin\phi \\ \sin\theta \end{pmatrix} \cdot \begin{pmatrix} \mathbf{u}(z) \\ w \end{pmatrix} \tag{11a}$$

$$\theta = \theta_0 + \frac{s}{\frac{4}{3}R_E} \tag{11b}$$

where ϕ direction from the radar to the disdrometer site (in the Cartesian coordinate system of the 4D-DSD model); θ is the local radar scan elevation angle above the disdrometer; θ_0 is the radar scan elevation angle relative to the radar site; s is the distance along the earth's surface from radar site to disdrometer site; and R_E is the average earth radius, 6371 [km]. The last term in Equation (11b) takes into account the curvature of the earth, while the factor of 4/3 accounts for radar refraction. Equation (11b) assumes that the radar and disdrometer sites are both at points on a perfect spherical earth of radius R_E.

Since under most conditions, the vertical component of $U_r(z)$ is very small compared to the horizontal component, setting $\theta = 0$ simplifies the simulated radial velocity. Combining Equations (10) and (11) with $\theta = 0$ yields:

$$U_r(z) \approx u_r(z) = u_0\left(\gamma + (1-\gamma)\tanh\frac{z - z_0}{L_z}\right)\cos(\phi - \psi) \tag{12}$$

In order to compare the model radial velocities from Equation (12) to the NEXRAD radial velocities V_r, such as those in Table 2, a vertical integration needs to be performed over the radar beam width at each elevation angle:

$$\begin{aligned}\overline{u}_r(m) &= \frac{1}{z_{m2} - z_{m1}}\int_{z_{m1}}^{z_{m2}} u_r(z) \\ &= u_0\left(\gamma + (1-\gamma)\frac{L_z}{z_{m2} - z_{m1}}\log\left(\cosh\frac{z_0 - z_{m2}}{L_z}\cdot\operatorname{sech}\frac{z_0 - z_{m1}}{L_z}\right)\right)\cos(\phi - \psi)\end{aligned} \tag{13}$$

where z_{m1} and z_{m2} are the bottom and top edges of the beam at the mth radar beam elevation angle.

The average advection velocity $\overline{\mathbf{u}}(m)$ the mth radar beam elevation angle can be estimated by plotting equal dBZ contours between consecutive scans, such that the contour lines bracket the disdrometer site. It is necessary to use the appropriate contour, corresponding to the dBZ value passing over the ground site at each scan time. For example, Figure 14 shows the NEXRAD 5 dBZ reflectivity contour for the m = 1 scan (lowest elevation scan) centered over the disdrometer site for the 19:04 and 19:08 UTC scans. The procedure depicted in Figure 14 can be repeated for all elevation angles of interest and for all time scans of interest.

Once the Z-contour velocities $\overline{\mathbf{u}}_C(m)$ have been estimated from the radar Z data, for at least m = 1, self consistency of the radar data can be checked by comparing the radial components of $\overline{\mathbf{u}}_C(m)$ with the Doppler radial velocities from Table 2. The radial component of $\overline{\mathbf{u}}_C(m)$ are determined by taking the dot product with the direction vector from the radar, similar to Equation (11). This comparison provides some confidence of the integrity of the radar derived advection data. In some cases, the Doppler radial velocity may be unreliable because and spatial and temporal fluctuations. The Z-contour derived advection may be unreliable in some cases, such as

during collisions of the sea breeze and front boundary movement, in which case advection may be undefined. For the purpose of disdrometer spatial and temporal interpolation-extrapolation of drop size distributions, the $\overline{\mathbf{u}}_C(m)$ may be a better measure of relevant advection. For example, during times a convective cell is stationary, $\overline{\mathbf{u}}_C(m)$ would most likely be a better indicator than the associated Doppler velocities.

The goal of the discussion of the last several paragraphs is to choose the best parameters for the advection model, Equations (10), based on empirical fitting to the Doppler and reflectivity derived horizontal air motion at the first two or three elevations angles. For example, the advection model corresponding to the 19:04 UTC radar scan is shown in Figure 15. It should be noted that the advection model of Equation (10a) only has the ability to change the velocity magnitude, not the direction. It can however, reverse the sign. Increasing the capabilities of the advection model would be a candidate for future work.

GENERALIZED LAGRANGIAN RAINFALL MODEL

The previous two sections described independent horizontal and vertical trajectory models of falling rain drops due to gravity and the effects of ambient air motion. The primary effect of atmospheric air motion is due to drag forces that either move the particle along with the ambient air and/or limit the drop fall velocity, i.e. terminal velocity. Other effects include particle lift due to the rotation of the particle or rotation of the gas around the particle. Lift forces, which may be positive or negative, are always in the direction of the gravity vector and are proportional to the horizontal component of drag. Lift is usually much smaller in magnitude than drag forces, except in the case of very fast rotations. Mass loss or gain is another affect that controls the detailed motion of rain drops. Evaporation, collisions, spontaneous breakup, and coalescence are mechanisms that further complicate drop dynamics.

A traditional approach to simulating trajectories of single particles in a gas flow is to employ a recursive integration algorithm such as the fourth order Runge-Kutta (RK4) algorithm, to compute the particle position at each time step. The inputs to the integration algorithm include local gas velocity vector, density, viscosity, and temperature at each of the particle's time-stepped positions. For some applications such as aeronautics, these gas properties might be output from a *computation fluid dynamics* (CFD) or *direct simulation Monte Carlo* (DSMC) model of the gas flow. Advanced fluid mechanics models utilize a two-way coupled system where the gas flow is affected by the particle flow, and the particle flow is in turn affected by the gas flow. Less computationally intensive software systems implement a one-way coupled model where the gas flow affects the particle flow, but the particle flow has no affect on the gas flow.

The horizontal advection and vertical wind components of falling rain can be combined in a one-way coupled algorithm, using physical property formulas of the surrounding air as input to the Lagrangian trajectory integration. For a hydrometeor of diameter D and mass m, the trajectory is due to the external forces: gravity, vertical updrafts/downdrafts, and advection. The sum of external forces on a hydrometeor is equal to its acceleration, which can be estimated by a Taylor series expansion about time point n, resulting in a set of difference equations for position and velocity (see Appendix C for a RK4 implementation):

$$\mathbf{v}_n = \mathbf{v}_{n-1} + \mathbf{a}_{n-1}\Delta t \qquad (14a)$$

$$\mathbf{r}_n = \mathbf{r}_{n-1} + \mathbf{v}_{n-1}\Delta t + \tfrac{1}{2}\mathbf{a}_{n-1}\Delta t^2 \tag{14b}$$

$$\mathbf{U}_n = \mathbf{U}(\mathbf{r}_n) = \begin{pmatrix} \mathbf{u}(\mathbf{r}_n) \\ w(\mathbf{r}_n) \end{pmatrix} \tag{14c}$$

$$\begin{aligned} \mathbf{a}_n &= \frac{\pi C_D D^2}{8m}\left|\mathbf{U}_n - \mathbf{v}_n\right|\cdot(\mathbf{U}_n - \mathbf{v}_n)\rho_n + g_E\hat{\mathbf{e}}_E \\ &= \frac{\pi C_D D^2}{8}\left(\frac{\pi D^3 \rho_H}{6}\right)^{-1}\left|\mathbf{U}_n - \mathbf{v}_n\right|\cdot(\mathbf{U}_n - \mathbf{v}_n)\rho_n + g_E\hat{\mathbf{e}}_E \\ &= \frac{3 C_D \rho_n}{4 D \rho_H}\left|\mathbf{U}_n - \mathbf{v}_n\right|\cdot(\mathbf{U}_n - \mathbf{v}_n) + g_E\hat{\mathbf{e}}_E \end{aligned} \tag{14d}$$

where g_E is earth gravity (9.80665 [m s^{-2}]) ; ρ_H is hydrometeor density (997.0479 [kg m^{-3}] at 25 C); $\rho(\mathbf{r}_k)$ is the air density; and $\mathbf{U}(\mathbf{r}_k)$ is the total air velocity at the *k*th time step particle position $\mathbf{r}_k$. The direction of the gravity unit vector $\hat{\mathbf{e}}_E$ is given by:

$$\begin{aligned} \hat{\mathbf{e}}_E &\equiv \frac{-1}{\sqrt{x^2 + y^2 + (R_E + x)^2}}\begin{pmatrix} x \\ y \\ R_E + z \end{pmatrix} \\ &\approx \begin{pmatrix} 0 \\ 0 \\ -1 \end{pmatrix} \qquad \text{for } x,y,z << R_E \end{aligned} \tag{15}$$

The coefficient of drag, C_D is a function of the Reynolds number, Re:

$$Re_n = \frac{D\rho_n\left|\mathbf{U}_n - \mathbf{v}_n\right|}{\mu_n} \tag{16}$$

where μ_n is the dynamic viscosity of air and is related to temperature by:

$$\mu_k = \mu(\mathbf{r}_k) = \mu_0 \frac{T_0 + C}{T(\mathbf{r}_k) + C}\left(\frac{T(\mathbf{r}_k)}{T_0}\right)^{3/2} \tag{17}$$

where $\mu_0 \equiv 1.827\times10^{-5}$ [Pa s], $T_0 \equiv 291.15$ [K], and $C_0 \equiv 120$ [K].

The air density ρ_n in Equation (14d) and (16) is related to temperature and air pressure:

$$\rho_n = \frac{P(\mathbf{r}_n)M_0}{R^* T(\mathbf{r}_n)} \tag{18a}$$

$$P(\mathbf{r}_n) = P_0\left(1 - \frac{\eta\, z_n}{T(0)}\right)^{\frac{g_E M_0}{R^* \eta}} \tag{18b}$$

$$T(\mathbf{r}_n) = T(0) - \eta\, z_n \tag{18c}$$

where M_0 is the molecular weight of dry air, equal to 0.0289644 [kg mol^{-1}]; R^* is the gas constant, equal to 8.31432 [J mol^{-1} K^{-1}]; P_0 is standard air pressure at sea level, equal to 101325 [Pa]; η is the average rate of temperature change with altitude, equal to 0.0065 [K m^{-1}]; and $T(0)$ is the standard temperature at sea level, equal to 288.15 [K].

The coefficient of drag is computed from the following empirical formula:

$$C_D = \begin{cases} 24.0Re^{-1} & Re < 2 \\ 18.5Re^{-0.6} & 2 \le Re < 500 \\ 0.44 & Re \ge 500 \end{cases} \tag{19}$$

The initial conditions assume that the hydrometeor is at terminal fall velocity:

$$\mathbf{v}_0 = \begin{pmatrix} \mathbf{u}(\mathbf{r}_0) \\ w - v_D \end{pmatrix}, \quad \mathbf{r}_0 = \begin{pmatrix} x_0 \\ y_0 \\ z_0 \end{pmatrix} \tag{20}$$

where the drop terminal velocity v_D is given by an approximation that accounts for of altitude effects, such as Best (1950) (see Equation A.16) in Appendix A.

Equations (14) through (20) define a complete Lagrangian trajectory model for hydrometeors, one that provides a method to integrate the equations of motion, following the hydrometeor path from an arbitrary stating point $\mathbf{r}_0 = (x_0, y_0, z_0)$ to the ground. The time of travel $\tau = L\Delta t$ is found by noting the number of time steps L where $\mathbf{r}_L \to (x_L, y_L, 0)$. The general strategy is to choose a set of starting points $\mathbf{r}_{0i}$, then run the trajectory Equations (14) – (20) recursively until the hydrometeor hits the ground., repeating this for a all discrete values of drop diameter D_j of the relevant drop size range. For every D_j starting at $\mathbf{r}_{0i}$, the coordinates on the ground and the arrival time at the ground is logged. The times and locations of the hydrometeor ground strikes are then related to the disdrometer spectra by a time delay and spatial extrapolation from the disdrometer location to the location of the hydrometeor strike. This procedure provides a method to generate a volume drop size distribution (DSD) in 3D space and in time. The Lagrangian approach to computing a 4D-DSD from the disdrometer data is a powerful method since it can easily accommodates complex spatial and temporal advection functions, as well as complex vertical wind profile functions. In previous work, a 3D-DSD algorithm was implemented in FORTRAN 95 to process disdrometer data using a set of ballistic equations which had been integrated analytically using simple functions of advection and vertical wind motion (Lane, 2000), where the wind motion was assumed to be time independent over the period of drop trajectory calculations. The Lagrangian trajectory method has no requirement of time

independent wind motion. (Note that the difference in terminology adopted in this work is that previous work computed a 3D-DSD where time was involved only in the trajectory equations, but was not used to compute changes in acceleration as a function of time).

DISDROMETER DERIVED REFLECTIVITY

A final problem to solve is that of spatial extrapolation from the disdrometer site to the point on the ground of the hydrometeor strike. An ad hoc approach is to assume that each *j*th-*k*th bin of the disdrometer histogram H_{jk} travels from the disdrometer site to the hydrometeor impact point $\mathbf{p}_{ij} = (x_{ij}, y_{ij})$ using the following transformation (Lane, 2000):

$$t'_{ij} = t_i + \tau_{ij} - \frac{\mathbf{u}(0) \cdot \mathbf{p}_{ij}}{|\mathbf{u}(0)|^2} \tag{21}$$

where $\mathbf{u}(0)$ is the advection velocity near the ground at $z \approx 0$; $\mathbf{p}_{ij}$ is the point of impact on the ground for the *j*th drop size falling from the $\mathbf{r}_{0i}$ position in space; τ_{ij} is the fall time of the *j*th drop size from the point $\mathbf{r}_{0i}$; and t_i is the absolute time that drops begin to fall from the point $\mathbf{r}_{0i}$. The disdrometer data corresponding to $H_{jk'}$ is then used to estimate the extrapolated disdrometer spectra at the hydrometeor impact point $\mathbf{p}_{ij}$, where:

$$k' = Int\left[\frac{t'_{ij} - t_0}{\Delta t}\right] \tag{22}$$

and t_0 is the absolute start time of the disdrometer spectra acquisition that produces $H_{jk'}$.

For the purpose of comparing disdrometer reflectivity to radar reflectivity, it is convenient to define the set of $\mathbf{r}_{0i}$ and t_i corresponding to the set of radar bins over the disdrometer volume, as shown in Figure 6.

In some cases, such as times when a sea breeze collides with a convective cell front, advection may not be well defined. In such cases where advection goes to zero or reverses direction, the last term on the right (the advection term) in Equation (22) can be deleted, which essentially reduces to the case of Equation (7b). In cases where advection is non-zero, but small or simply not consistent, a linear combination of these two solutions can then be used to compute the drop size distribution:

$$N(D) = \beta\, N_a(D) + (1 - \beta)\, N_s(D) \tag{23}$$

where β is an empirical parameter that mixes some percentage of the advective case $N_a(D)$ defined by Equation (22) and the stationary non-advective case, $N_s(D)$ of Equation (7b).

DISCUSSION AND SUMMARY

Referring to the plots in Tables 1 and 3, the 19:04 and 19:08 scans show a distinct improvement in the disdrometer derived reflectivity when vertical fall time is incorporated into the processing algorithm (second and third columns compared to the first column). The Lagrangian-advection

model, shown in the middle column of Table 3 also shows good agreement with the radar in most cases. Scans 19:13, 19:18, and 19:23 all show good agreement in all columns with the corresponding radar reflectivity. One explanation for this behavior is that during the 19:13 – 19:23 period, rainfall is characterized by a very broad pulse, so that gravitational sorting is not a significant effect during that time interval (refer to the disdrometer spectra plot of Figure 4 at 780 – 1380 [s]). In this case, the disdrometer reflectivity can easily track the radar reflectivity.

Scans 19:28, 19:33, and 19:38 begin to show severe disagreement between disdrometer and radar. Only the processing methods shown in Table 4 display reasonable agreement with the radar reflectivity. An explanation for this case is that the rainfall is characterized by impulsive conditions (refer to Figure 4 at 1680 – 2280 [s]). During this time, advection begins to degenerate due to interaction of the storm movement with surrounding opposing winds (this is somewhat apparent in the radar data). Another symptom of poorly defined advection is seen in Table 4, by examining the evolution of the mixing parameter β. Recall from Equation (23) that $\beta = 1$ is a purely advective solution, whereas $\beta = 0$ is a purely non advective solution defined by Equation (7b). In Table 4, where all parameters are created by a manual process of finding a best fit to the corresponding radar plot, $\beta = 1$ during the non-impulsive phase, then begins to decreases to smaller values. The only exception, β during the 19:04 scan is less than 1, which may be explained by poor advection conditions at the earliest approach of the storm, when rainfall rate and reflectivity are very small.

Another interesting feature in the parameter set of Table 4 is the evolution of the vertical velocity parameter w. Vertical velocity starts out at a small value or negative (downdraft), then begins to rise to larger and larger positive values (updraft), where the maximum coincides with the maximum radar reflector at 19:23.

Methods to improve disdrometer processing, loosely based on mathematical techniques common in the field of particle flow and fluid mechanics, have been explored. The inclusion of advection and vertical winds appears to produce significantly improved results, in spite of very strict assumption of non-interacting hydrometeors, constant vertical air velocity, and time independent advection during the scan time interval. Future work should focus on relaxing these assumptions by developing at the least a simple model of drop interaction. Time dependent advection may be incorporated quite simply within the frame work of the Lagrangian trajectory mechanics.

A most important activity of future work should be to exercise the model vigorously with a sufficient volume of data so that statistics of the model performance can be quantified. Along with this effort, all available independent wind field data should be rigorously collected and processed to be used as inputs into the Lagrangian model. Sources of this data may be derived directly from each radar elevation scan by plotting and analyzing reflectivity contours over the disdrometer site, such as that demonstrated in Figure 14, and by collecting the radar radial velocity data. Strong GS signatures in the disdrometer spectra are another potential source of vertical wind data. Other sources of data that would be very useful, if available - nearby anemometer or wind tower data. Rain gauge data from multiple gauges positioned within a kilometer or less of the disdrometer site would provide a valuable addition to the set of data required 4D-DSD optimization and verification.

REFERENCES

D. A. Shepard, "A Two-Dimensional Interpolation Function for Irregularly-Spaced Data", 23th National Conference of the Association for Computing Machinery, Brandon/Systems Press, Inc., Princeton, NJ, pp. 133-145, 1968.

J. S. Marshall and W. M. Palmer, "The Distribution of Raindrops with Size," *Journal of Meteorology*, **9**, pp. 327-332, 1948.

J.E. Lane, D.W. Sharp, T.C. Kasparis, and N.J. Doesken, 2008: "Hail disdrometer array for launch systems support", Preprints, 13th Conference on Aviation, Range and Aerospace Meteorology, Amer. Meteor. Soc., New Orleans, LA, CD-ROM P2.10.

Lane, J. E., P. T. Metzger, et al. (2008), "Lagrangian trajectory modeling of lunar dust particles", Earth and Space 2008, Long Beach, CA.

A. C. Best, "Empirical Formula for the Terminal Velocity of Water Drops Falling Through the Atmosphere", *Quarterly Journal of the Royal Meteorological Society*, Vol. 75, pp. 302-311, 1950.

Lane, J., Kasparis, T., Jones, W. L.; Merceret, F. and B. Muller, "Radar Volume Reflectivity Estimation using an Array of Ground Based Rainfall Drop Size Detectors", SPIE Proc. AeroSense 2000, April 24-29, 2000, Orlando, FL.

C. W. Ulbrich, "Natural Variations In the Analytical Form of the Raindrop-Size Distribution", *Journal of Climate and Applied Meteorology*, Vol. 22, pp. 1764-1775, 1983.

J. O. Laws, "Measurements of the Fall-Velocity Of Water-Drops and Raindrops", *Transactions of the American Geophysical Union*, Vol. 22, pp. 709-721, 1941.

E. K. Edgarton and J. R. Killian, *Flash: Seeing the Unseen by Ultra High Speed Photography*, Hale Publishing Co., 1939.

H. R. Pruppacher and K. V. Beard, "A Wind Tunnel Investigation of the Internal Circulation and Shape of Water Drops Falling at Terminal Velocity In Air", *Quarterly Journal of the Royal Meteorological Society*, Vol. 96, pp. 247-256, 1970.

R. Gunn and G. D. Kinzer, "The Terminal Velocity of Fall for Water Droplets In Stagnant Air", *Journal of Applied Meteorology*, Vol. 6, pp. 243-248, 1948.

D. Atlas, R. C. Srivastava, and R. S. Sekhon, "Doppler Radar Characteristics of Precipitation at Vertical Incidence", *Review of Geophyics and Space Physics*, Vol. 2, pp. 1-35, 1973.

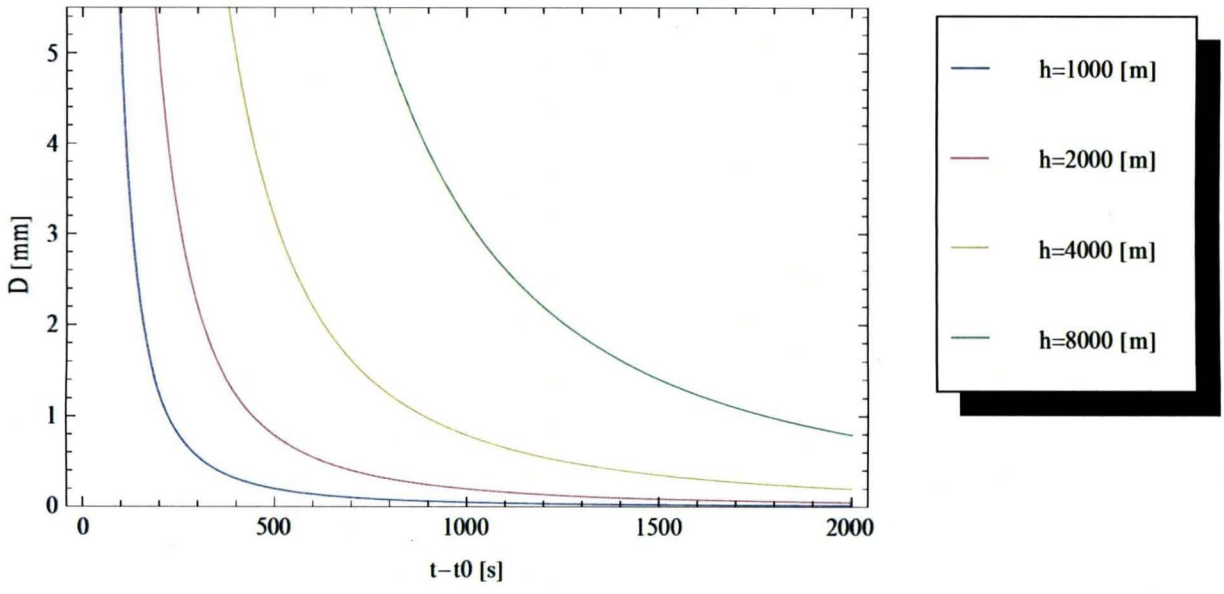

Figure 1. Plots of $D(t)$ due to idealized pulse rain characterized by a delta function, using Equation (2) for various values of h with $w = 0$.

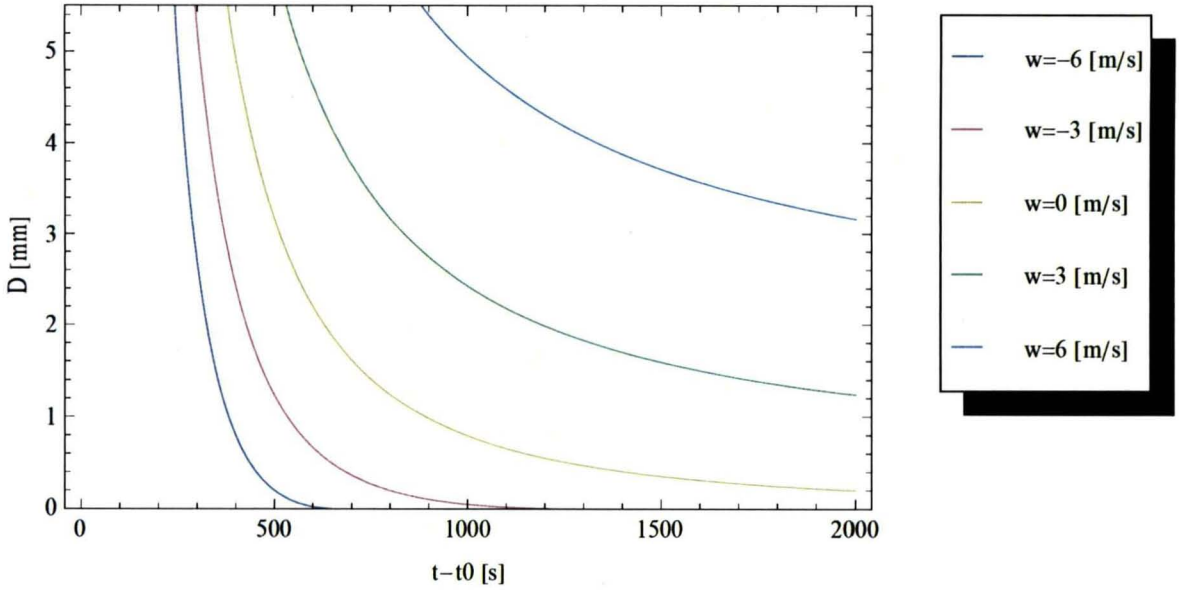

Figure 2. Plots of $D(t)$ due to idealized pulse rain characterized by a delta function, using Equation (2) for various values of w with $h = 2000$ [m].

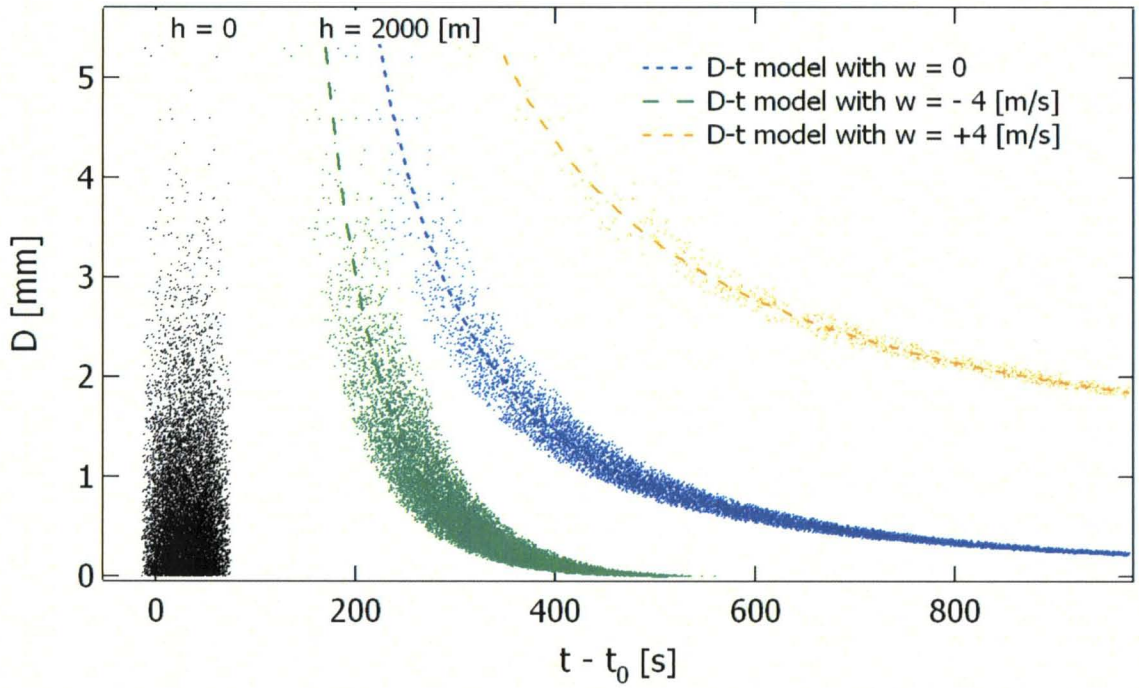

Figure 3. Simulated disdrometer data for a $\tau = 60$ [s] pulse of $R = 100$ [mm/h] rainfall using 10^6 Monte Carlo drops generated with a MP drop size distribution.

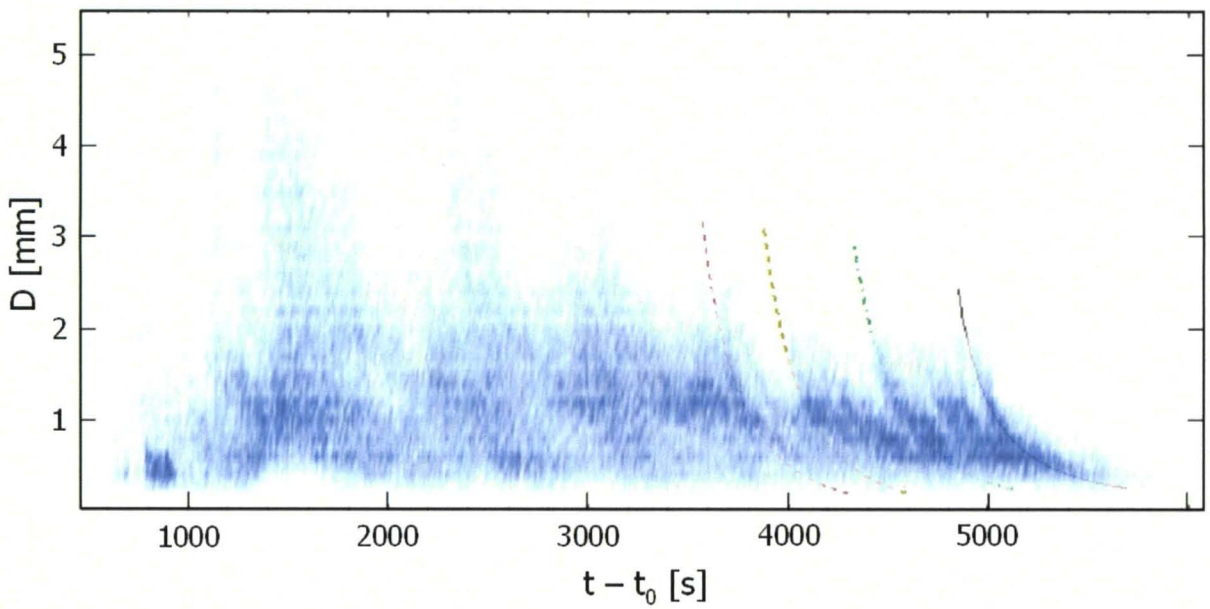

Figure 4. Joss disdrometer data from the UCF site, September 30, 2008, with t_0 = 19:00 UTC. $D(t)$ plotted is from Equation (2): dashed line, w = -1.5 [m/s], h = 4000 [m]; thick dashed line, w = -1.5 [m/s], h = 4000 [m]; dot-dashed line, w = -1.0 [m/s], h = 4000 [m]; solid line, w = +0.5 [m/s], h = 2000 [m].

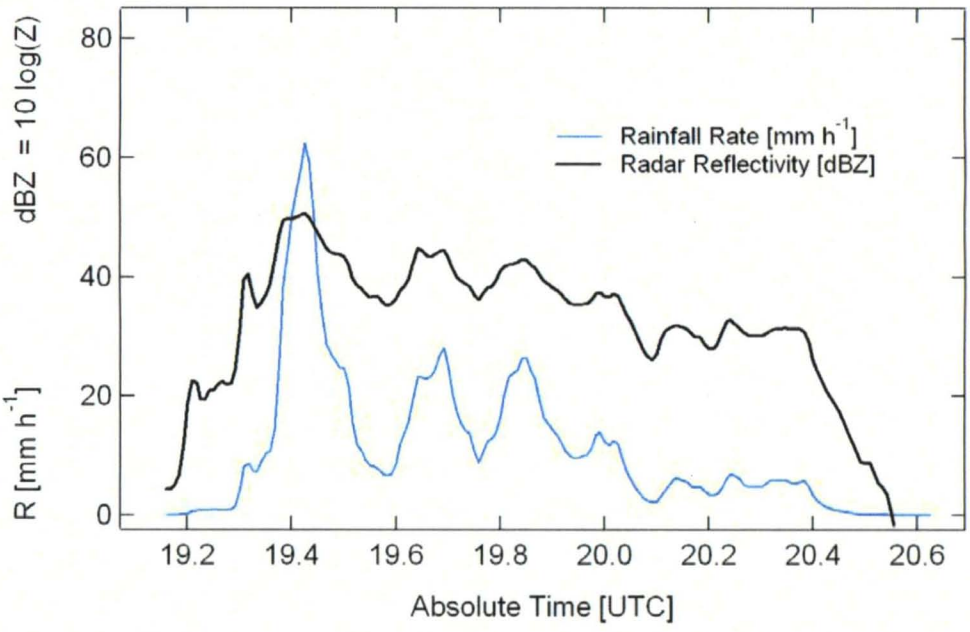

Figure 5. Rainfall products derived from September 30, 2008 Joss disdrometer at UCF: thin line is rainfall rate computed by Equation (4); thick line is equivalent radar reflectivity computed using Equation (5).

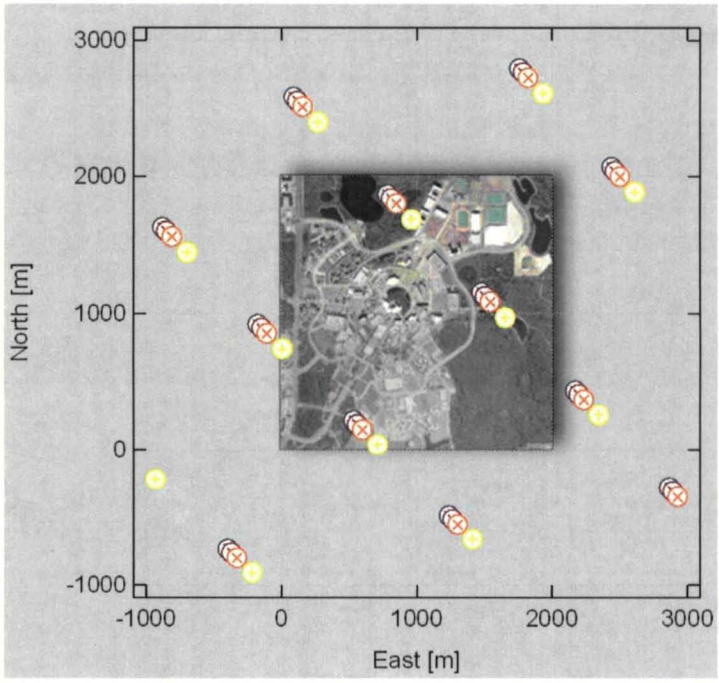

Figure 6. UCF disdrometer site (Joss disdrometer in located in center). Circles represent locations of the Melbourne NWS radar bins for the lowest four elevations (09-30-08): black circles, $z = 1.00$ [km], $t = 19{:}24{:}06$ UTC; brown circles, $z = 2.40$ [km], $t = 19{:}24{:}41$ UTC; red circles, $z = 3.50$ [km], $t = 19{:}25{:}23$ UTC; and yellow circles, $z = 4.90$ [km], $t = 19{:}25{:}45$ UTC.

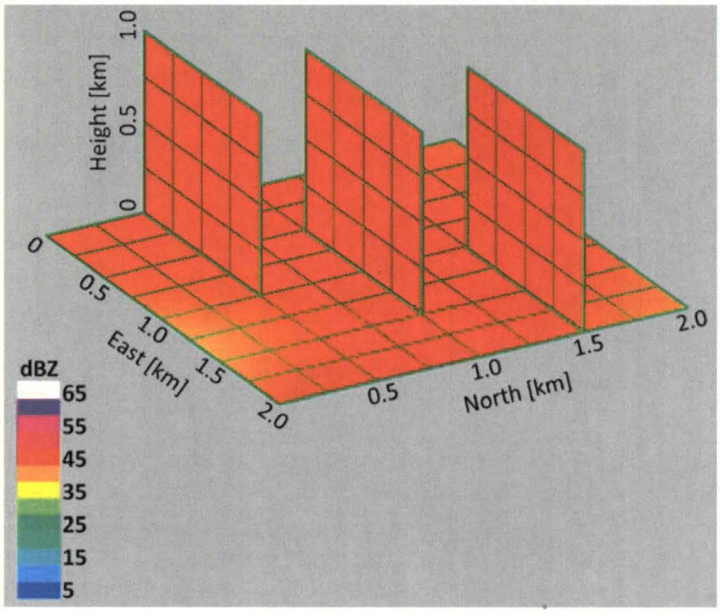

Figure 7. *3DRadPlot* of Melbourne radar reflectivity over UCF Joss site, 09-30-08, 19:23 UTC.

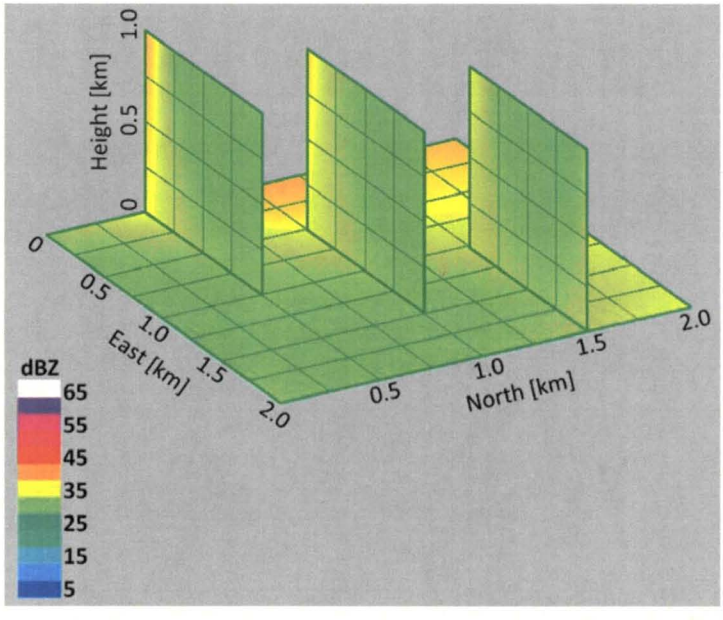

Figure 8. *3DRadPlot* of Melbourne radar reflectivity over UCF Joss site, 09-30-08, 19:38 UTC.

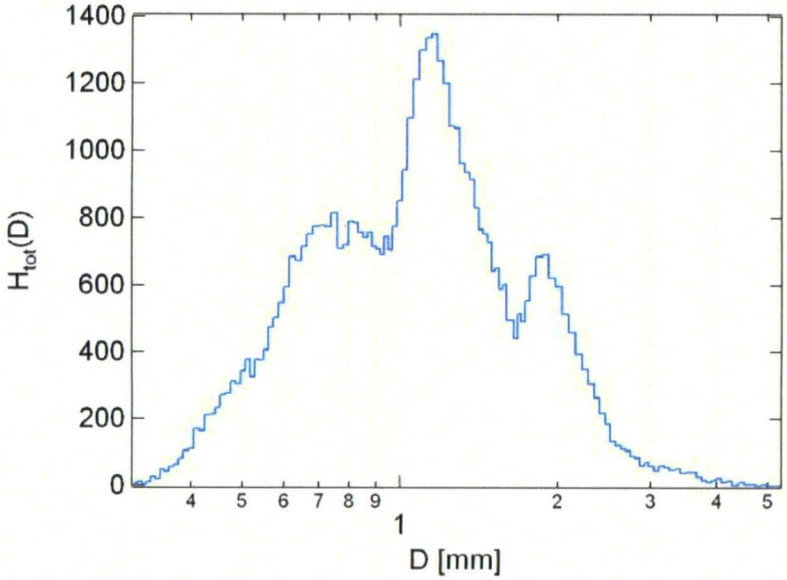

Figure 9. Joss histogram corresponding to Figure 4, summed over all k time intervals.

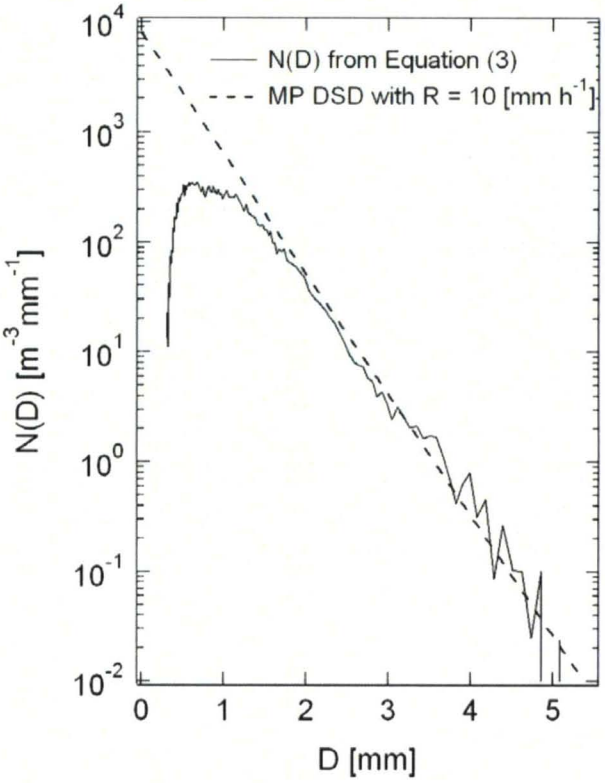

Figure 10. Joss derived drop size distribution using Equation (3), for entire storm event of Figure 4, with $\Delta t = 6000$ [s]. The MP DSD equivalent corresponds to an average rainfall rate of 10 [mm h^{-1}]

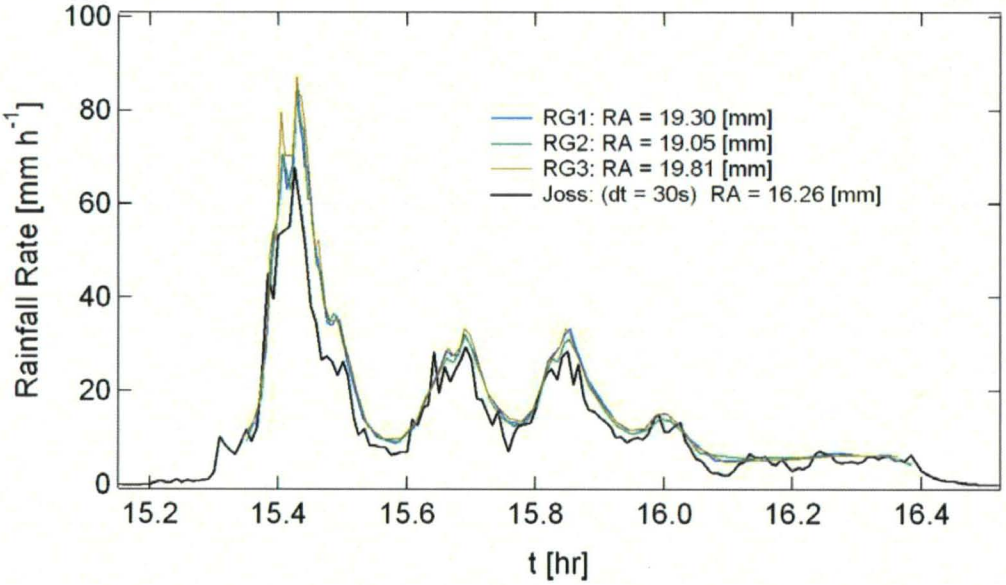

Figure 11. Thick line is rainfall rate derived from the Joss data using Equation (4) with $\Delta t = 30$ [s]. The three thin lines are rainfall rate measured by three collocated rain gauges. The total storm accumulated gauge rainfall average is 19.39 [mm], as compared to the 16.26 [mm] for the Joss.

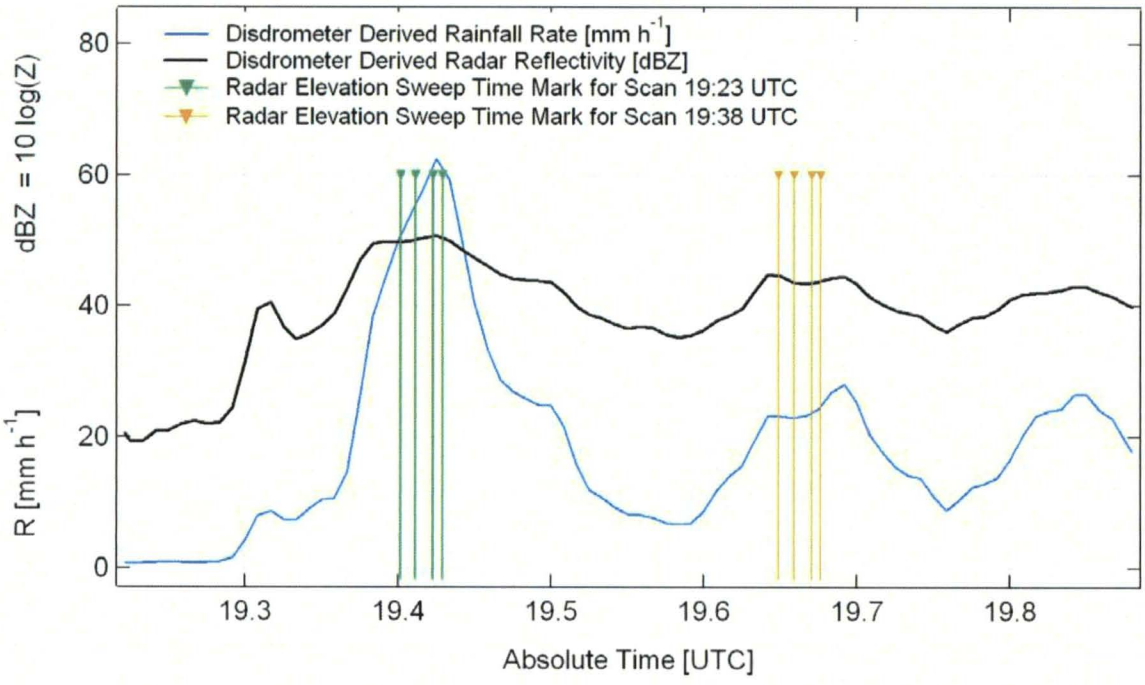

Figure 12. Close-up of disdrometer derived reflectivity corresponding to the lowest four elevation scans over the UCF site (refer to Figure 6) for 19:23 UTC and 19:38 UTC scans with time marks. The average Z for 19:23 UTC is 50.1 dBZ and 43.9 dBZ for 19:38 UTC. This should be compared to the reflectivity values shown by the NEXRAD data of Figures 7 and 8.

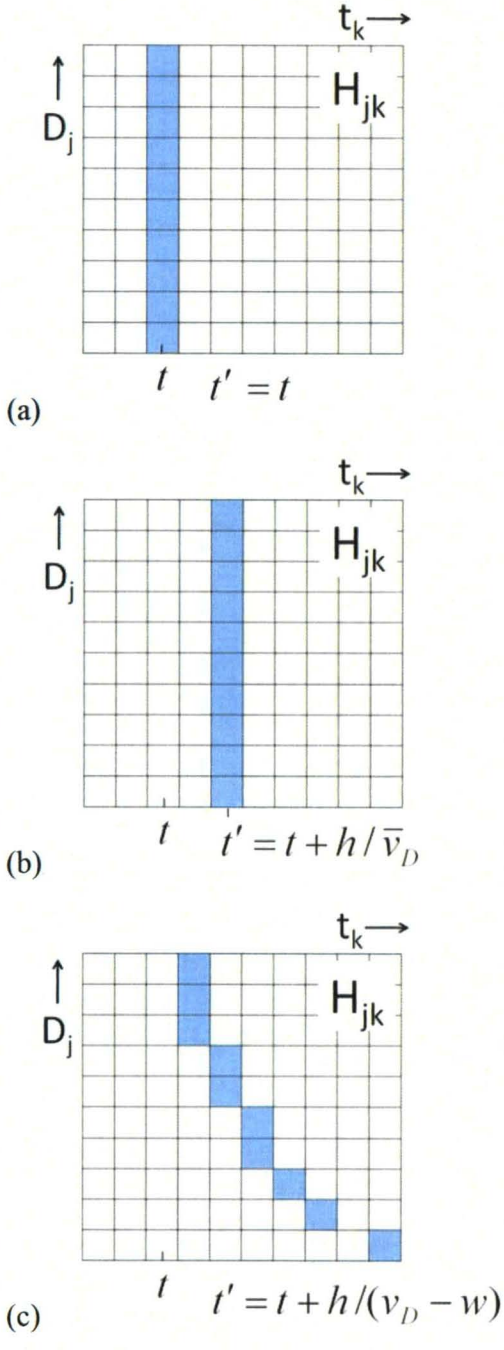

Figure 13. Comparison strategies for radar reflectivity Z and disdrometer derived reflectivity Z': (a) *simple* case where the time t of the radar scan is matched to the corresponding disdrometer data at $t' = t$; (b) the *simple time delay* case where $Z(t)$ is matched to the disdrometer data delayed by the average drop terminal velocity $\bar{v}_D$ falling from a height $z = h$; (c) *GS time delay* case where the time delay is dependent on the terminal velocity v_D of each drop size as well as vertical air velocity w.

Table 1. Application of Equations (9a)-(9c) to compute disdrometer derived Z with comparison to Melbourne equivalent radar reflectivity on a scan by scan basis, using UCF Joss data of September 30, 2008. Note that the simple case shown in the first column was actually produced by setting w = -999 [m s^{-1}] in Equations (9).

Disdrometer derived reflectivity Z using simple case of Figure 13a and Equation (5).	Disdrometer Z using method of Figure 13c and Equations (9) with w set 0.	Disdrometer Z using method of Figure 13c and Equations (9) with manual optimization of w.	Melbourne NEXRAD reflectivity plotted in a 2x2x1 [km] volume centered over UCF Joss site.
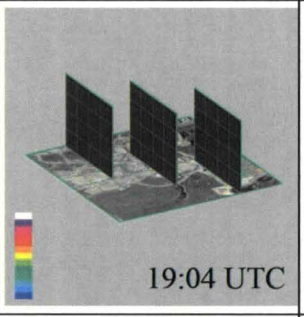	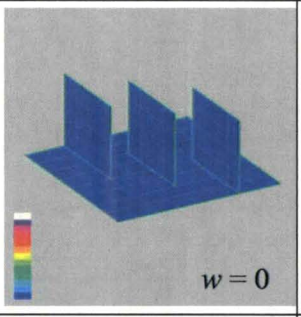	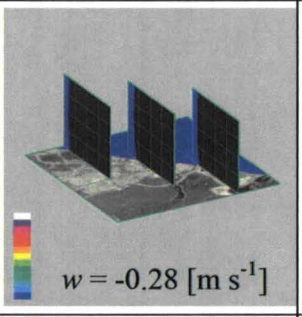	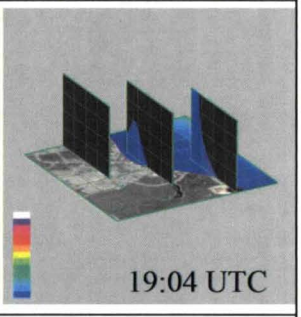
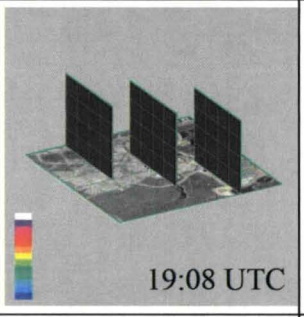	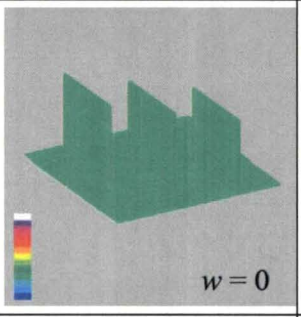	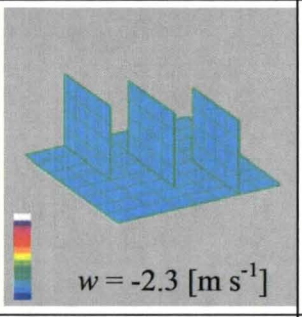	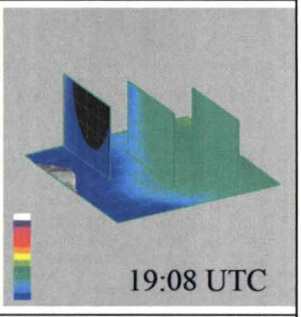
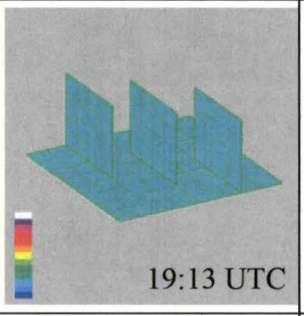	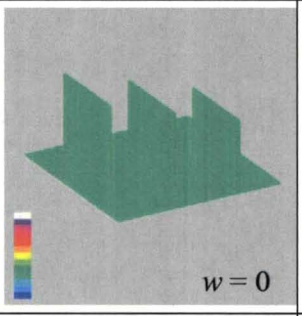	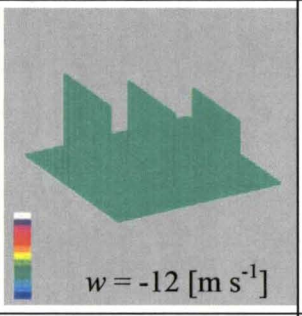	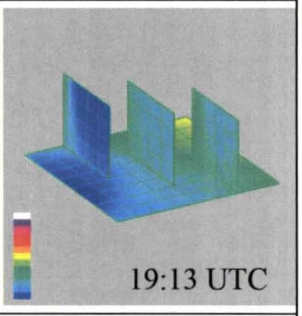
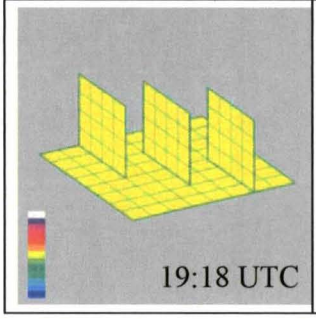	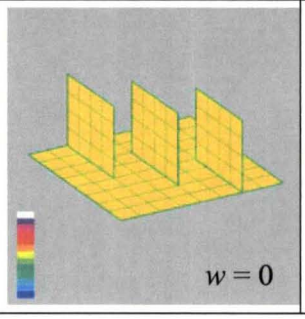	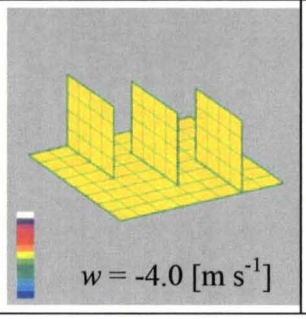	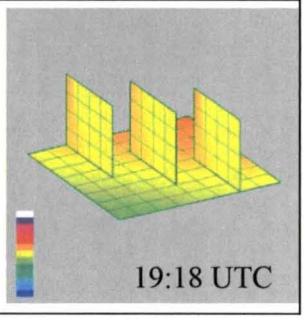

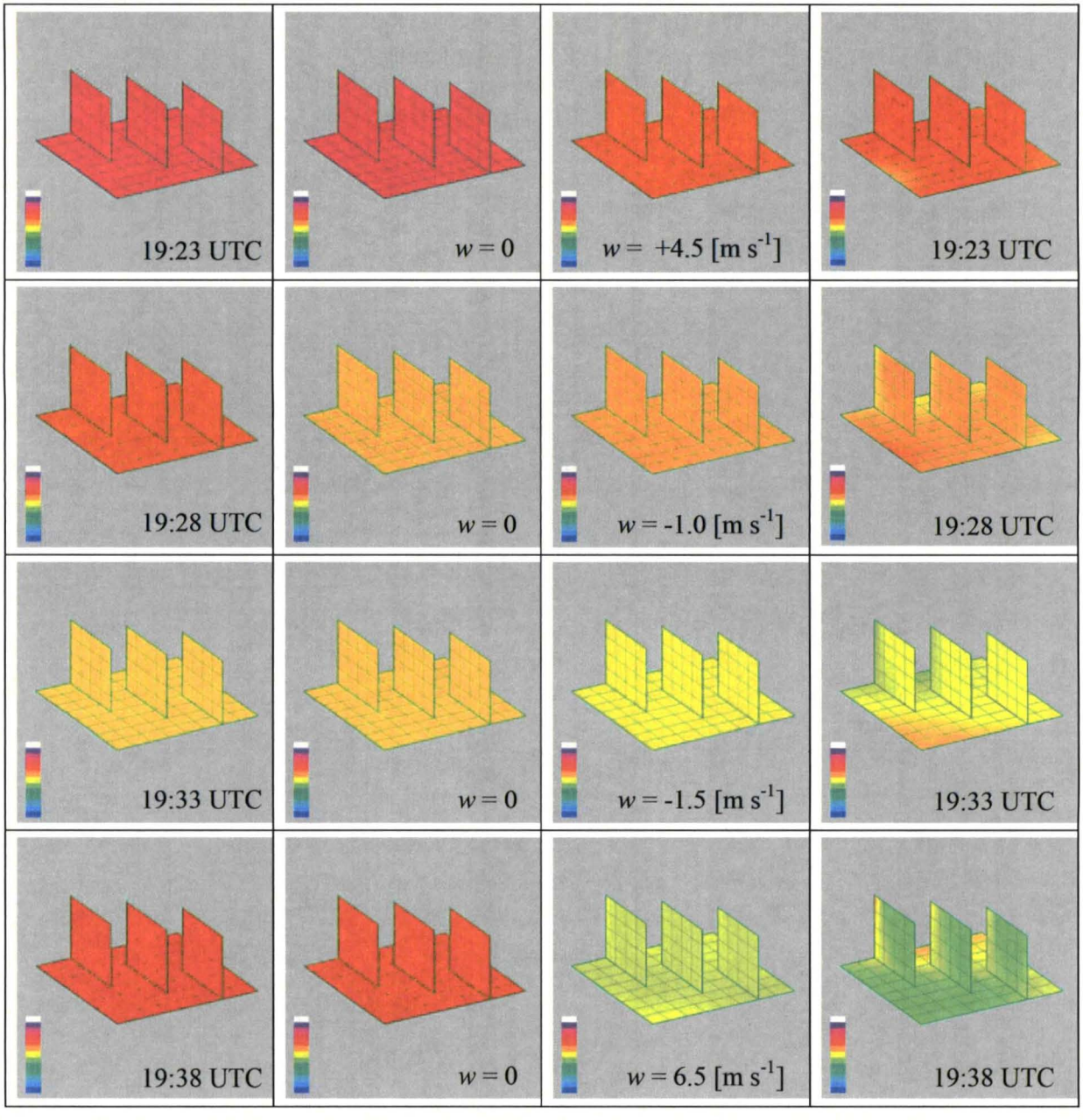
19:23 UTC
w = 0
w = +4.5 [m s-1]
19:23 UTC
19:28 UTC
w = 0
w = -1.0 [m s-1]
19:28 UTC
19:33 UTC
w = 0
w = -1.5 [m s-1]
19:33 UTC
19:38 UTC
w = 0
w = 6.5 [m s-1]
19:38 UTC

Table 2. Level II Melbourne NEXRAD radial velocity data over the UCF Joss disdrometer site, Septmeber 30, 2008.

t UTC	Elev [deg]	z [m]	Classified V_r [m/s]	Unclassified V_r [m/s]
19:04	0.47	959	-	-2.52056
	1.44	2246	-	-1.49176
	2.39	3511	-10.288	-5.50408
19:08	0.47	960	-5.144	-4.47528
	1.44	2246	5.144	1.49176
	2.39	3513	-5.144	-1.49176
19:18	0.47	960	-10.288	-6.01848
	1.44	2247	5.144	0.97736
	2.39	3512	9.7736	2.52056
19:23	0.47	962	-10.288	-8.02464
	1.44	2245	-5.144	-2.52056
	2.39	3515	5.144	0.5144
19:28	0.47	963	-10.288	-6.99584
	1.44	2246	5.144	1.49176
	2.39	3508	5.144	0.97736
20:22	0.47	963	-5.144	-4.47528
	1.43	2243	-5.144	-4.98968
	2.39	3513	-5.144	-3.49792
20:27	0.47	959	-5.144	-4.01232
	1.43	2242	-5.144	-4.47528
	2.39	3515	-5.144	-4.01232

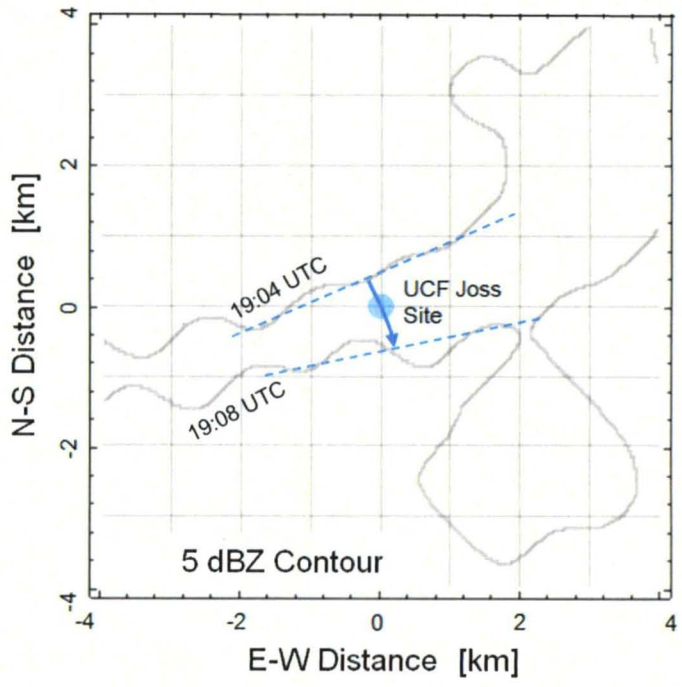

Figure 14. Lowest elevation angle plot of the Melbourne NEXRAD 5 dBZ reflectivity contour over the UCF disdrometer site. Based on the translation of the equal contour line, the corresponding advection velocity over the site, using the notation of Equation (13), is approximately $\overline{u}_C(1) \approx 3.3$ [m s^{-1}], with $\psi = -68°$.

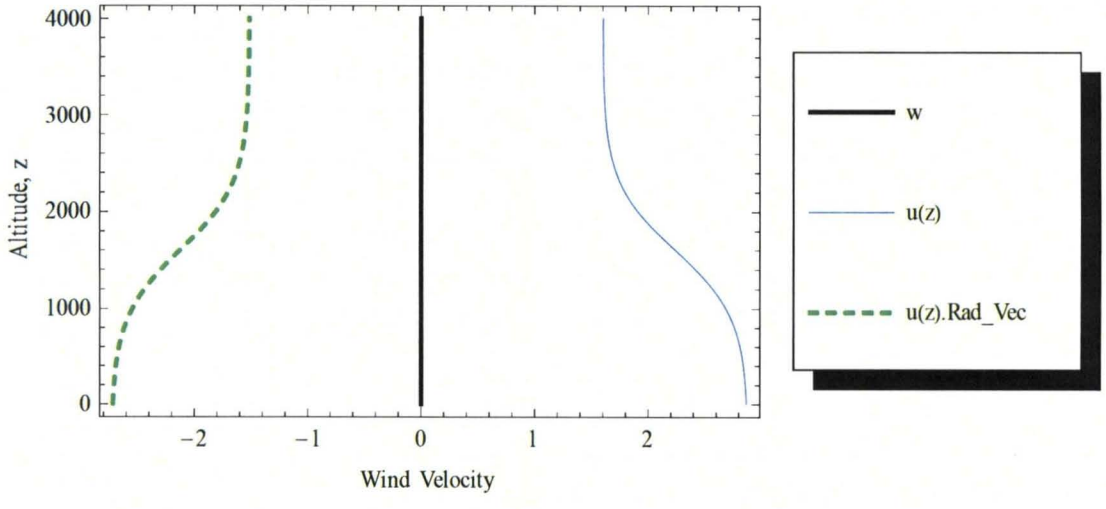

Figure 15. Advection model for scan 19:04 UTC from Equations (10), with $\gamma = 1.4$, $L_z = 700$ [m], $z_0 = 1600$ [m], $\psi = -64°$, $u_0 = 1.6$ [m s^{-1}], with $\phi = 134.5°$.

Table 3. Comparison of Lagrangian trajectory model disdrometer derived Z with Melbourne equivalent radar reflectivity on a scan by scan basis, using UCF Joss data of September 30, 2008. The first column is copied from the third column of Table 1.

Disdrometer Z using method of Figure 13c and Equations (9) with manual optimization of w.	Disdrometer Z using Lagrangian trajectory model and Equations (21)-(23) with manual optimization of all parameters (see Table 4).	Melbourne NEXRAD reflectivity plotted in a 2x2x1 [km] volume centered over UCF Joss site.
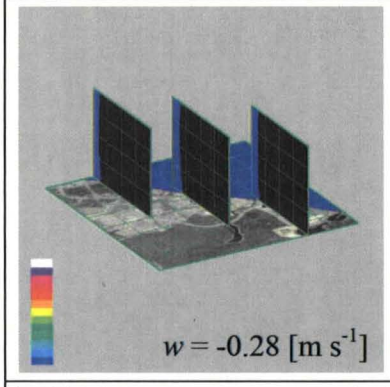	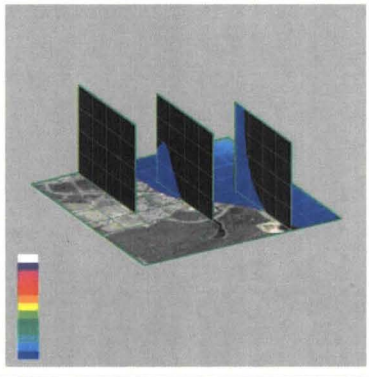	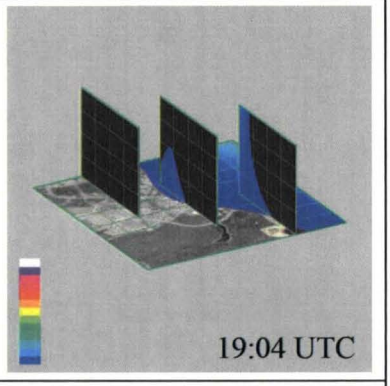
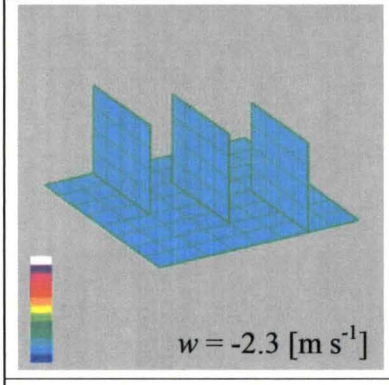	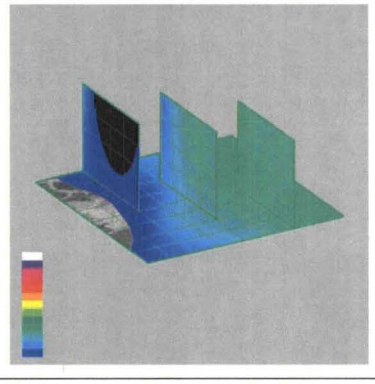	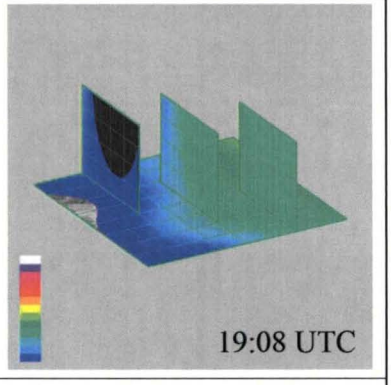
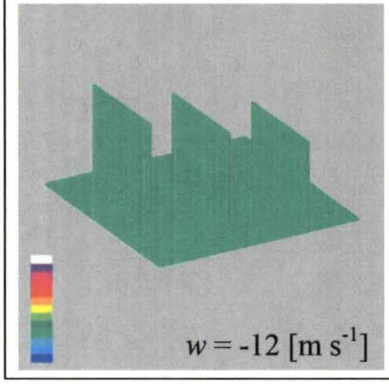	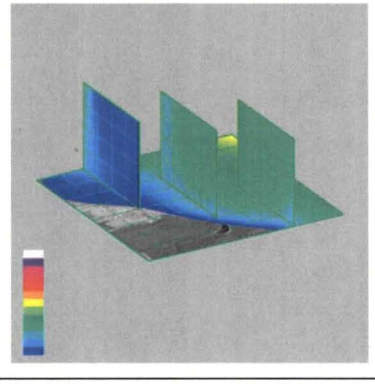	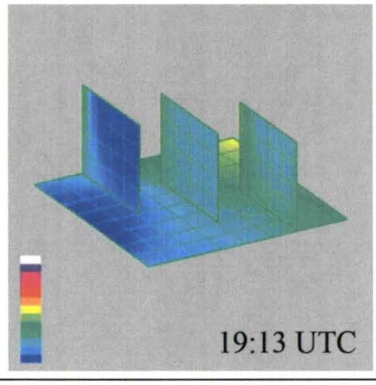

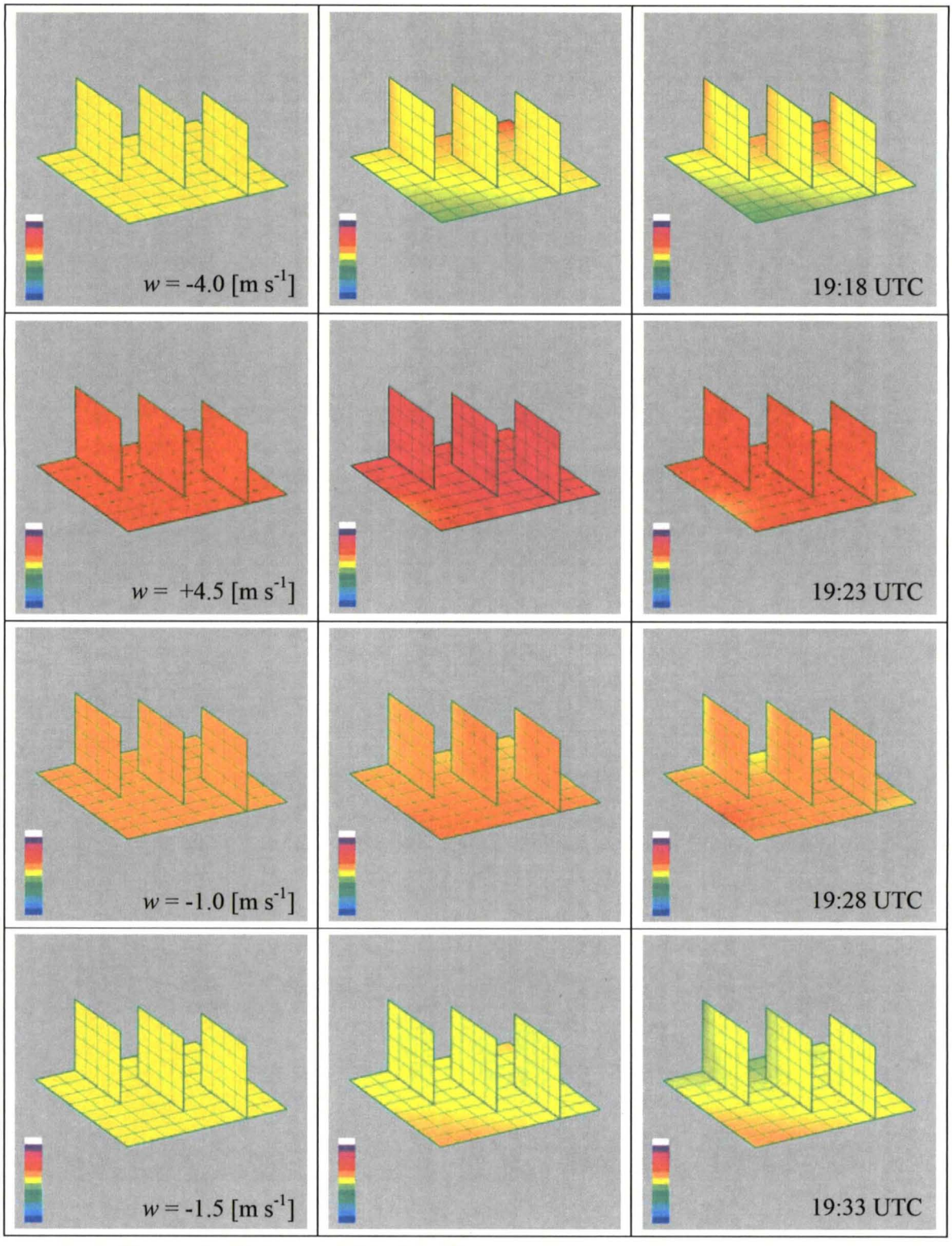
w = -4.0 [m s-1]
19:18 UTC
w = +4.5 [m s-1]
19:23 UTC
w = -1.0 [m s-1]
19:28 UTC
w = -1.5 [m s-1]
19:33 UTC

Table 4. Lagrangian model parameters used to produce second column in Table 3.

UTC Time	19:04	19:08	19:13	19:18	19:23	19:28	19:33
u_0 [m s^{-1}]	1.6	-1.3	6.2	-1.8	1.35	-1.6	5.5
ψ [deg]	-64	-99	-72	-43	-69	-35	-40
β	0.61	1.0	1.0	1.0	1.0	0.55	0.29
γ	1.4	-4.0	0.52	-7.7	4.2	-7.0	1.0
L_z [m]	700	920	350	800	850	600	500
z_0 [m]	1600	0	0	0	1500	600	0
w [m s^{-1}]	0	0	-2.5	1.0	4.5	4.0	-5.7

APPENDIX A

DROP SIZE DISTRIBUTION

The drop size distribution is the number of raindrop hydrometeors per unit volume per drop size diameter D. Usually the DSD is denoted by $N(D)$ and is expressed in units of m^{-3} mm^{-1} or cm^{-4}. The total number of drops N_T in a volume of air is equal to the integral of $N(D)$ over all drop diameters:

$$N_T = \int_0^\infty N(D)\, dD \tag{A.1}$$

where $N(D)dD$ is the number of drops per unit volume with diameters between D and $D + dD$.

Since the largest raindrop sizes found in nature do not exceed 6 to 7 mm, the DSD is often defined as:

$$DSD = \begin{cases} N(D) & D \le D_{MAX} \\ 0 & D > D_{MAX} \end{cases} \tag{A.2}$$

Quantities involving the DSD, such as N_T, are then found from the truncated integral:

$$N_T = \int_0^{D_{MAX}} N(D)\, dD \approx \int_0^\infty N(D)\, dD \tag{A.3}$$

For most quantities involving integrals of $N(D)$, the error associated with the choice of large drop size cutoff is insignificant as compared to errors from other sources. A practical strategy, which will be used in this work, is to limit large drop sizes to 6 mm when performing data analysis. When performing analytical calculations on integrals involving $N(D)$, it is more convenient to use infinity as the upper bound for drop size since in this case, the integrals often reduce to the form of a simple *gamma function*.

EXPONENTIAL DISTRIBUTION

The simplest and probably most commonly used DSD is the *exponential distribution*:

$$N(D) = N_0\, e^{-\Lambda D} \tag{A.4}$$

where N_0 and Λ are fitting parameters. In this case, the total number of drops per unit volume reduces to:

$$\begin{aligned} N_T &= \int_0^\infty N_0\, e^{-\Lambda D}\, dD \\ &= N_0\, \Lambda^{-1} \end{aligned} \tag{A.5}$$

GAMMA DISTRIBUTION

The *gamma distribution* (Ulbrich, 1983) was proposed in order to alleviate a problem at small drop diameters seen by researchers, which suggested that $N(D) \to 0$ as $D \to 0$:

$$N(D) = N_0 D^{\nu} e^{-\Lambda D} \tag{A.6}$$

The gamma distribution also allowed for a three parameter fit, where υ, as well as N_0 and Λ are the fitting parameters. In this case, the total number of drops per unit volume reduces to:

$$\begin{aligned} N_T &= \int_0^{\infty} N_0 D^{\nu} e^{-\Lambda D} \, dD \\ &= \frac{N_0}{\Lambda^{1+\nu}} \Gamma(1+\nu) \end{aligned} \tag{A.7}$$

Comparing Equations (A.4) and (A.5) to Equations (A.6) and (A.7), it can be seen that the exponential distribution is a special case of the gamma distribution where $\upsilon = 0$.

MARSHALL-PALMER DISTRIBUTION

The *Marshall-Palmer* (MP) DSD is a special case of the exponential distribution, described by Equation (A.4), where historically the exponential DSD may have resulted as a generalization of the MP DSD. The MP DSD is characterized by its explicit definition of the fitting parameters, N_0 and Λ:

$$\begin{aligned} N_0 &= 8000 \ \text{m}^{-3}\text{mm}^{-1} \\ \Lambda &= 4.1 \, R^{-0.21} \ \text{mm}^{-1} \end{aligned} \tag{A.8}$$

with R in units of mm h^{-1}. The original DSD data by Marshall and Palmer is shown in Figure A-1.

The total number of drops for the MP DSD, based on Equation (A.5), is:

$$\begin{aligned} N_T &= N_0 \Lambda^{-1} \\ &= (N_0 / 4.1) \, R^{0.21} \\ &= (1951.2) \, R^{0.21} \ \text{m}^{-3} \end{aligned} \tag{A.9}$$

According to the MP DSD and Equation (A.9), the total number of drops per unit volume increase as the 0.21 power of R.

RAINDROP TERMINAL VELOCITY

The equation of motion for a raindrop of mass m_D in a uniform gravitational field of acceleration g, falling in the z direction (defined positive from cloud to ground, where $z = 0$ at the initial starting point in the cloud), is:

$$m_D \ddot{z} = m_D g - \mu_D \dot{z}^2 \tag{A.10}$$

where the first term on the right-hand-side (RHS) is the gravitational force and the second term on the RHS is the force due to frictional drag through air. Approximations for the quantities in Equation (A.10) can be estimated by assuming a spherical drop shape of diameter D and by neglecting the change in atmospheric density with altitude:

$$m_D \approx \frac{\pi D^3 \rho_W}{6} \tag{A.11a}$$

$$\mu_D \approx \frac{\pi D^2 \rho C_d}{8} \tag{A.11b}$$

where ρ_W is the density of water, ρ is the density of air (neglecting altitude dependence), and C_d is the drag coefficient of a spherical drop. By substituting $v = \dot{z}$ in the equation of motion, Equation (A.10) becomes:

$$\begin{aligned} v\frac{dv}{dz} &= g - \frac{\mu_D}{m_D} v^2 \\ &= g\left(1 - v^2 / v_D^2\right) \end{aligned} \tag{A.12}$$

where $v_D \equiv \sqrt{m_D g / \mu_D}$. The solution to the differential equation of Equation (A.12) is:

$$v = v_D\left(1 - e^{-2gz/v_D^2}\right)^{1/2} \tag{A.13}$$

As $z \to \infty$ in Equation (A.13), $v \to v_D$, thus implying that v_D is the terminal velocity of a drop of diameter D. Experimental data (Laws, 1941) for drop velocities versus fall height for several drop sizes, is shown in Figure A-2, along with the velocities predicted by Equation (A.13). Note that Equation (A.13) also correctly predicts that as z goes to zero:

$$v \underset{z \to 0}{\to} (2gz)^{1/2} \tag{A.14}$$

which is the free fall solution in a vacuum, where the drag force vanishes.

One of the primary problems with the former arguments is the assumption that the raindrop shape is spherical. Figures A-3 and A-4 show high-speed photographs of drops at terminal velocity (Edgarton, 1939, and Pruppacher, 1970). For drop diameters larger than about 3 mm, the shape becomes more flattened as the diameter increases. For this reason, terminal velocity formulas are usually empirical and are not usually based on the spherical drop shape assumption of Equation (A.11b).

APPROXIMATION BY GUNN (1948)

A simple form of drop terminal velocity v_D is described by a simple power-law (Gunn, 1948):

$$v_D \approx K_G D^{1/2} \tag{A.15}$$

where $K_G = 4.5$ when drop diameter D is expressed in mm and terminal velocity is in units of m s^{-1}. This particular form of v_D is particularly useful when evaluating integrals over drop size, involving drop size distribution functions. Specific examples of this will be presented in sections to follow.

APPROXIMATION BY BEST (1950)

An improved approximation for terminal velocity (Best, 1950), which takes into account the variation of velocity with altitude, due to atmospheric density, is:

$$v_D \approx A e^{bz} \left\{ 1 - e^{-(D/a)^n} \right\} \tag{A.16}$$

where $A = 9.58$ m s^{-1}, $b = 0.0854$ km^{-1}, z is the elevation at the ground (or at the point of measurement), D is the drop diameter measured in mm, $a = 1.77$ mm, $n = 1.147$, and v_D is expressed in units of m s^{-1}.

APPROXIMATION BY ATLAS (1973)

Another approximation for terminal velocity (Atlas, 1973), which is also an improvement over the power-law form of Gunn, is:

$$v_D \approx v_0 \left(1 - K e^{-cD} \right) \tag{A.17}$$

where $v_0 = 9.65$ m s^{-1}, $K = 1.067$, c = 0.6 mm^{-1}, and D is expressed in mm. Even though this form of v_D is not as simple as Gunn's approximation, it nevertheless results in a form which is relatively easy to manage when evaluating integrals involving DSD functions.

MOMENTS OF THE DSD

Many useful atmospheric and meteorological quantities can be calculated simply by evaluating the xth moment of the DSD:

$$M_x = \int_0^\infty D^x N(D)\, dD \tag{A.18}$$

For example, the total number of drops N_T in a volume of air is equal to M_0, the zeroth moment of the DSD, as verified by Equation (A.1).

LIQUID WATER CONTENT

The third moment M_3 of the DSD is proportional to the amount of water in a unit volume of air:

$$V = \tfrac{\pi}{6}\rho_W \int_0^\infty D^3 N(D)\, dD$$
$$= \tfrac{\pi}{6}\rho_W M_3 \qquad \text{(A.19)}$$

If the exponential DSD described by Equation (A.5) is used to evaluate M_3, the result is:

$$V = \tfrac{\pi}{6}\rho_W N_0 \int_0^\infty D^3\, e^{-\Lambda D}\, dD$$
$$= \pi \rho_W N_0 \Lambda^{-4} \qquad \text{(A.20)}$$

where ρ_W is the density of water.

RAINFALL RATE

The integral over D of the product of terminal velocity and DSD is equal to the rainfall rate. If the terminal velocity v_D is described by Gunn's approximation, Equation (A.15), rainfall rate R becomes the 7/2 moment of the DSD:

$$R = \tfrac{\pi}{6} K_G \int_0^\infty D^{7/2} N(D)\, dD$$
$$= \tfrac{\pi}{6} K_G M_{7/2} \qquad \text{(A.21)}$$

where $K_G = 4.5$ (drop diameter D is expressed in mm and terminal velocity in units of m s^{-1}). If the exponential DSD of Equation (A.5) is used, R then evaluates to:

$$R = (0.0036)\tfrac{\pi}{6} K_G\, N_0 \int_0^\infty D^{7/2} e^{-\Lambda D}\, dD$$
$$= (0.0036)\tfrac{35}{32}\pi^{3/2} K_G\, N_0 \Lambda^{-9/2} \qquad \text{(A.22)}$$

where the scale factor 0.0036 places R in standard unit of mm h^{-1}.

RADAR REFLECTIVITY

The sixth moment M_6 of the DSD is approximately equal to the radar reflectivity:

$$Z = \int_0^\infty D^6 N(D)\, dD$$
$$= M_6 \qquad \text{(A.23)}$$

If the exponential DSD of Equation (A.5) is used, Z then evaluates to:

$$Z = N_0 \int_0^{\infty} D^6 e^{-\Lambda D}\, dD$$
$$= 720\, N_0 \Lambda^{-7} \qquad \text{(A.24)}$$

where Z is in standard units of $mm^6\ m^{-3}$. Note that a commonly used measure of Z is $dBZ = 10\ \log_{10}(Z)$.

Z-R RELATION

The rainfall rate R described by Equation (A.22) can be combined with the radar reflectivity Z given by Equation (A.24), by eliminating Λ:

$$Z = \left(\frac{274211}{K_G^{14/9}\ N_0^{5/9}} \right) R^{14/9} \qquad \text{(A.25)}$$

Using $K_G = 4.5$ and $N_0 = 8000$, Z becomes:

$$Z = a\, R^b \qquad \text{(A.26)}$$

where $a \approx 179.3$ and $b = 14/9 \approx 1.56$. Equation (A.26) is a *Z-R* relation derived from Gunn's terminal velocity and the exponential DSD. Equation (A.26) is the well known *Z-R* power law used to convert weather surveillance radar (WSR) data to estimations of rainfall amounts. However, it should be noted that the National Weather Service (NWS) has adopted the modified values of $a = 300$ and $b = 1.4$ for use with its WSR-88D radar network.

APPENDIX B

3D-MAPPING OF NWS REFLECTIVITY DATA

3DRadPlot was originally developed to compare NWS NEXRAD volume reflectivity data to drop size distribution data acquired from a cluster of disdrometers. In this work, particular attention was given to studying data from a cluster of hail disdrometers and the corresponding radar data: http://www.nasa.gov/mission_pages/shuttle/behindscenes/hail_monitor.html. Additional information concerning spatial interpolation and extrapolation of disdrometers is included in the \Papers directory from the 3DRadPlot page at openchannelsoftware.com. However, *3DRadPlot* plots radar data only, even though the development was motivated by plotting the 3D data from the disdrometer cluster.

NCDC NEXRAD DATA INVENTORY

Radar data from all NWS NEXRAD sites is archived at the National Climatic Data Center (NCDC). That data can be readily accessed at http://www.ncdc.noaa.gov/nexradinv/. *3DRadPlot* plots Level III reflectivity data at four scan elevations. These files are denoted by the sub-string, N0R, N1R, N2R, and N3R. A complete file name is for example:

```
7000KMLB_SDUS52_N0RMLB_200702262214.txt
```

corresponding to Melbourne radar data, lowest elevation scan, of February 26, 2007, 2214:00 UTC. The additional three elevation scans that are available from Level III data, for this particular case, turn out to be:

```
7000KMLB_SDUS22_N1RMLB_200702262214.txt
7000KMLB_SDUS22_N2RMLB_200702262214.txt
7000KMLB_SDUS32_N3RMLB_200702262214.txt
```

These are binary files. After ordering the data from the date and time of interest, the following message will indicate that data is ready for *pickup*. The files are then downloaded by clicking on the link in an email message, such as the following:

```
From: Orders HAS [mailto:orders@thunder.ncdc.noaa.gov]
Sent: Sunday, August 26, 2007 2:28 PM
To: john.lane@ksc.nasa.gov
Subject: HAS Data Request: HAS001184684 Completed

Your request (HAS001184684) has completed. The procedure to ftp the data is as
follows:

http://www1.ncdc.noaa.gov/pub/has/HAS00118468

NOTE: You must pick up your data within 7 days of this notice.

Thank you,

National Climatic Data Center
E-mail: NCDC.Orders@noaa.gov
Internet:  www.ncdc.noaa.gov
```

RADFILES.TXT

The *.txt files downloaded from the NCDC ftp site are listed by the user, using a text editor, in *RadFiles.txt*.

```
 1. Pad-A_8x8k_S.bmp
 2.   28.5723  -80.6452
 3. 7000KMLB_SDUS52_N0RMLB_200702262214.txt  10000.0
 4. 7000KMLB_SDUS22_N1RMLB_200702262214.txt  10000.0
 5. 7000KMLB_SDUS22_N2RMLB_200702262214.txt  10000.0
 6. 7000KMLB_SDUS32_N3RMLB_200702262214.txt  10000.0
 7. #
 8. Zxy1.dat            Zxy2.dat              40     200      10
 9. Zxz1.dat            Zxz2.dat              40     100    4000
10. Zyz1.dat            Zyz2.dat              40     100    4000
```

Using the above file as an example, the following notes can be generalized to other cases:

- Line 1 is a bitmap image supplied by the user of the *x-y* plane background, sized to a 200 × 200 pixel image. The image represents a square plot region whose dimensions correspond to the product of the third and fourth entries in line 8 in meters.
- The lat/lon of the lower left corner of the plot region (southwest corner) is given in line 2.
- Lines 3 – 6 are the files downloaded via the NCDC ftp server described in the previous section. Note that not all four elevations are required. Any combination can be listed, but must be in vertical ascending order. The numerical parameter which follows the filename is the distance in meters from the region origin (given by line 2) that will define the region to be processed for plotting. Note that this value may be equal to or greater than the plot region spatial extent.
- Line 7 marks the end of the radar data file name entries. One to four entries are valid.
- Line 8 is the *x-y* plane parameters. The first string defines an output file that contains the *x* (north-south), *y* (east-west), and dBZ data, where dBZ is the radar reflectivity data. A spatial interpolation has been performed on the data contained in this file. The second file name corresponds to similar plot data, but without spatial interpolation. The third entry is *x-y* plot cell size in meters. The fourth entry is the number of cells, as discussed previously, the product of these two values defines the extent of the plot region in the *x-y* plane. The last parameter is the z position (elevation) in meters of the *x-y* plot plane.
- Line 9 is the *x-z* plane parameters. The first string defines an output file that contains the *x* (north-south), *z* (elevation), and dBZ data. A spatial interpolation has been performed on the data contained in this file. The second file name corresponds to similar plot data, but without spatial interpolation. The third entry is *x-z* plot cell size in meters. The fourth entry is the number of cells, where the product of these two values defines the extent of the plot region in the *x-z* plane. The last parameter is the *y* position (north-south position) in meters of the *x-z* plot plane.
- Line 10 is the *y-z* plane parameters. The first string defines an output file that contains the *y* (east-west), *z* (elevation), and dBZ data. A spatial interpolation has been performed on the data contained in this file. The second file name corresponds to similar plot data, but without spatial interpolation. The third entry is *y-z* plot cell size in meters. The fourth entry is the number of cells, where the product of these two values defines the extent of the plot region in the *y-z* plane. The last parameter is the *x* position (east-west position) in meters of the *y-z* plot plane.

SITE_COORD.DAT

This input file contains the lat/lon of three disdrometer sites. There is no processing done in *3DRadPlot* requiring this data, other than small marks inserted in the 2D data plot files, corresponding to these site locations.

Note: *This file must exist with three entries, but the data contained within is not used by 3DRadPlot. This file is not at all necessary or relevant unless disdrometer data is to be plotted by another application (not included here).*

OUTPUT FILES

- *Arga.dat* – this file corresponds exactly to the coordinates in *Site_Coord.dat* but is represented by *x-y* values, in meters, from the origin of the *x-y* plot region, defined by line 1 of *RadFiles.txt*.
- *Log.dat* – this file contains miscellaneous information extracted from the Level III files, as well as processing comments. This file can be used for debugging.
- Six 2D plot output files, corresponding to the six names given in lines 8-10 of *RadFiles.txt.*
- *Pnnnn.dat* – contains the *x*, *y*, *z*, and *t* volume scan cell coordinates defined by the bounding box formed from the plot origin, line 2, and the region extent entry in lines 3-6 of *RadFiles.txt.* This file contains the 4D coordinates which would be used in the disdrometer interpolation/extrapolation for comparison to the radar data.
- *Z3D.bmp* – is a bitmap 3D plot of the 2D data. The colors represent dBZ increments of 5, starting with 5, ending with 65.

EXECUTABLE

The executable is:

3DRadPlot.exe

If all input files are in place, execution of the above file will generate the output files described above.

APPENDIX C

4th ORDER RUNGE-KUTTA FOR 2ND ORDER DIFFERENTIAL EQUATIONS

$$
\begin{aligned}
\boldsymbol{\alpha}_1 &= \mathbf{v}_{n-1}\Delta t \\
\boldsymbol{\beta}_1 &= \mathbf{x}_{n-1} + \tfrac{1}{2}\boldsymbol{\alpha}_1 \\
\boldsymbol{\gamma}_1 &= \mathbf{a}(n\Delta t, \mathbf{x}_{n-1}, \mathbf{v}_{n-1})\Delta t \\
\boldsymbol{\delta}_1 &= \mathbf{v}_{n-1} + \tfrac{1}{2}\boldsymbol{\gamma}_1 \\
\\
\boldsymbol{\alpha}_2 &= \boldsymbol{\delta}_1\Delta t \\
\boldsymbol{\beta}_2 &= \mathbf{x}_{n-1} + \tfrac{1}{2}\boldsymbol{\alpha}_2 \\
\boldsymbol{\gamma}_2 &= \mathbf{a}((n+\tfrac{1}{2})\Delta t, \boldsymbol{\beta}_1, \boldsymbol{\delta}_1)\Delta t \\
\boldsymbol{\delta}_2 &= \mathbf{v}_{n-1} + \tfrac{1}{2}\boldsymbol{\gamma}_2 \\
\\
\boldsymbol{\alpha}_3 &= \boldsymbol{\delta}_2\Delta t \\
\boldsymbol{\beta}_3 &= \mathbf{x}_{n-1} + \boldsymbol{\alpha}_3 \\
\boldsymbol{\gamma}_3 &= \mathbf{a}((n+\tfrac{1}{2})\Delta t, \boldsymbol{\beta}_2, \boldsymbol{\delta}_2)\Delta t \\
\boldsymbol{\delta}_3 &= \mathbf{v}_{n-1} + \boldsymbol{\gamma}_3 \\
\\
\boldsymbol{\alpha}_4 &= \boldsymbol{\delta}_3\Delta t \\
\boldsymbol{\gamma}_4 &= \mathbf{a}((n+1)\Delta t, \boldsymbol{\beta}_3, \boldsymbol{\delta}_3)\Delta t \\
\mathbf{x}_n &= \mathbf{x}_{n-1} + \tfrac{1}{6}(\boldsymbol{\alpha}_1 + 2\boldsymbol{\alpha}_2 + 2\boldsymbol{\alpha}_3 + \boldsymbol{\alpha}_4) \\
\mathbf{v}_n &= \mathbf{v}_{n-1} + \tfrac{1}{6}(\boldsymbol{\gamma}_1 + 2\boldsymbol{\gamma}_2 + 2\boldsymbol{\gamma}_3 + \boldsymbol{\gamma}_4)
\end{aligned}
\qquad \text{(C.1)}
$$

http://www.physics.orst.edu/~rubin/nacphy/ComPhys/DIFFEQ/mydif2/